The Astronomical Journal, 164:29 (23pp), 2022 July https://doi.org/10.3847/1538-3881/ac73f4

Improved Orbital Constraints and Hα Photometric Monitoring of the Directly Imaged Protoplanet Analog HD 142527 B

William O. Balmer[1,2,3], Katherine B. Follette[3], Laird M. Close[4], Jared R. Males[4], Robert J. De Rosa[5], Jéa I. Adams Redai[6], Alex Watson[3], Alycia J. Weinberger[7], Katie M. Morzinski[4], Julio Morales[8], Kimberly Ward-Duong[9], and Laurent Pueyo[1,2]
[1] Department of Physics & Astronomy, Johns Hopkins University, 3400 N. Charles Street, Baltimore, MD 21218, USA; wbalmer1@jhu.edu
[2] Space Telescope Science Institute, 3700 San Martin Drive, Baltimore MD 21218, USA
[3] Department of Physics & Astronomy, Amherst College, 25 East Drive, Amherst, MA 01002, USA
[4] Steward Observatory, University of Arizona, Tucson, 933 N Cherry Avenue, Tucson, AZ 85721, USA
[5] European Southern Observatory, Alonso de Córdova 3107, Vitacura, Santiago, Chile
[6] Center for Astrophysics, Harvard & Smithsonian, 60 Garden Street, Cambridge, MA 02138, USA
[7] Earth & Planets Laboratory, Carnegie Institution for Science, 5241 Broad Branch Road NW, Washington, DC 20015, USA
[8] Department of Astronomy, University of Massachusetts, Amherst, MA 01003, USA
[9] Department of Astronomy, Smith College, Northampton, MA 01063, USA
Received 2021 September 6; revised 2022 May 25; accepted 2022 May 25; published 2022 July 1

Abstract

Companions embedded in the cavities of transitional circumstellar disks have been observed to exhibit excess luminosity at Hα, an indication that they are actively accreting. We report 5 yr (2013–2018) of monitoring of the position and Hα excess luminosity of the embedded, accreting low-mass stellar companion HD 142527 B from the MagAO/VisAO instrument. We use `pyklip`, a Python implementation of the Karhunen–Loeve Image Processing algorithm, to detect the companion. Using `pyklip` forward modeling, we constrain the relative astrometry to 1–2 mas precision and achieve sufficient photometric precision (±0.2 mag, 3% error) to detect changes in the Hα contrast of the companion over time. In order to accurately determine the relative astrometry of the companion, we conduct an astrometric calibration of the MagAO/VisAO camera against 20 yr of Keck/NIRC2 images of the Trapezium cluster. We demonstrate agreement of our VisAO astrometry with other published positions for HD 142527 B, and use `orbitize!` to generate a posterior distribution of orbits fit to the relative astrometry of HD 142527 B. Our data suggest that the companion is close to periastron passage, on an orbit significantly misaligned with respect to both the wide circumbinary disk and the recently observed inner disk encircling HD 142527 A. We translate observed Hα contrasts for HD 142527 B into mass accretion rate estimates on the order of $4\text{–}9 \times 10^{-10}\,M_{\odot}\,\mathrm{yr}^{-1}$. Photometric variation in the Hα excess of the companion suggests that the accretion rate onto the companion is variable. This work represents a significant step toward observing accretion-driven variability onto protoplanets, such as PDS 70 b&c.

Unified Astronomy Thesaurus concepts: Direct imaging (387); Stellar accretion (1578); Accretion (14); Star formation (1569); Orbit determination (1175)

1. Introduction

As the circumstellar environment surrounding young pre-main-sequence stars evolves, forming planets and binary companions disrupt and shape the circumstellar disk (e.g., Williams & Cieza 2011; Dong & Fung 2017). Embedded giant planets (protoplanets) and binary companions are expected to play dramatic roles in the formation of substructures such as cavities, rings, and spiral features within disks (e.g., Dodson-Robinson & Salyk 2011; Bae et al. 2018). In the past two decades, improvements in high-contrast imaging instrumentation and post-processing techniques have revealed these morphologically complex disks in striking detail (e.g., Tamura 2016; Avenhaus et al. 2018; Esposito et al. 2020; Garufi et al. 2020). Of particular interest are so-called "transition disks" (Dodson-Robinson & Salyk 2011; Espaillat et al. 2014), which host a wide central cavity depleted of dust. Gas has been observed to flow through these cavities (Casassus et al. 2013), fueling accretion onto the central star as well as onto the planetary (e.g., Sallum et al. 2015; Wagner et al. 2018; Haffert et al. 2019; Zhou et al. 2021) and stellar (Close et al. 2014a) mass companions that may be responsible for clearing them. This accretion is likely mediated by a circumsecondary (or circumplanetary) disk, observational evidence of which is accumulating at NIR (e.g., Lacour et al. 2016) and submm (e.g., Benisty et al. 2021) wavelengths.

Cleared central cavities and ongoing accretion make transition disks prime targets for visible light adaptive optics imaging searches for forming protoplanets. Accreting companions are expected to exhibit substantial Hα excess emission during accretion (Mordasini et al. 2017; Szulágyi & Ercolano 2020; Aoyama et al. 2021). This enables their detection at lower contrasts than non-accreting objects. Taking images through Hα and nearby continuum filters simultaneously and subtracting them allows for measurement of the Hα luminosity of the accreting object through Simultaneous-Spectral Differential Imaging (S-SDI). So far, few[10] embedded, accreting

[10] Aside from HD 142527 B, there are a total of four candidate accreting objects currently known to orbit *within* transitional disk cavities. They include the (disputed) candidate LkCa 15b: $M_{\rm p} < 5 - 10 M_{\rm J}$, $M_p \dot{M} \sim 10^{-6} M_J^2\,\mathrm{yr}^{-1}$ (Sallum et al. 2015; Currie et al. 2019), confirmed planet PDS 70 b: $M_{\rm p} \sim 4\text{–}10 M_{\rm J}$, $\dot{M} \sim 5 \times 10^{-7} M_{\rm J}\,\mathrm{yr}^{-1}$ (Keppler et al. 2018; Wagner et al. 2018; Haffert et al. 2019; Hashimoto et al. 2020; Wang et al. 2021), confirmed planet PDS 70 c: $M_{\rm p} \sim 4 - 12 M_{\rm J}$, $\dot{M} \sim 1 \times 10^{-8} M_{\rm J}\,\mathrm{yr}^{-1}$ (Haffert et al. 2019; Wang et al. 2021), and candidate AB Aur b: $M_{\rm p} \sim 9 - 12 M_{\rm J}$ (Currie et al. 2022).

companions have been directly imaged at Hα, with recent surveys returning no new detections (Cugno et al. 2019; Zurlo et al. 2020). This may be a low Strehl selection effect (Close 2020) or a reflection of differences in accretion physics at planetary masses (Aoyama et al. 2021; Marleau et al. 2022).

2. HD 142527

HD 142527 is a well-studied transitional disk system at a distance of 159.3 ± 0.7pc (Gaia Collaboration et al. 2021). The central star, HD 142527 A, is a young (5.0 ± 1.5 Myr; Mendigutía et al. 2014) F6III-V type Herbig Ae/Be star with an estimated mass of $M_A = 2.0 \pm 0.3\,M_\odot$ (Mendigutía et al. 2014). It exhibits accretion on the order of $10^{-7}\,M_\odot\,\mathrm{yr}^{-1}$ that is variable by at least a factor of 7 over $\sim$5 yr (Mendigutía et al. 2014). The system has a low extinction ($A_v = 0.0^{+0.05}_{-0.00}$; Fairlamb et al. 2015). The outer disk surrounding HD 142527 A is moderately inclined ($i_{\rm disk} = 28\overset{\circ}{.}0 \pm 0\overset{\circ}{.}5$; Perez et al. 2015; Boehler et al. 2017), hosts spiral arms in both scattered light (e.g., Fukagawa et al. 2006; Avenhaus et al. 2014; Hunziker et al. 2021) and submm gas emission (e.g., Boehler et al. 2021; Garg et al. 2021), and exhibits an asymmetrical "horseshoe" of submm thermal emission (e.g., Ohashi 2008; Boehler et al. 2017). The central cavity of the disk is heavily depleted of dust (Avenhaus et al. 2017) and extends to $\sim$140 au (Avenhaus et al. 2014). Gas emission within the cavity exhibits a complex morphology, with a possible warp in the innermost region (Casassus et al. 2013, 2015; Perez et al. 2015) and non-Keplerian motion throughout (Garg et al. 2021).

The inner thermally emitting disk component was first inferred by SED modeling of NIR excess and unresolved submillimeter observations (Verhoeff et al. 2011; Boehler et al. 2017). Narrow "shadow" features have been observed along the outer disk cavity wall, suggesting that this inner disk may be inclined with respect to the outer disk (Marino et al. 2015). Bohn et al. (2022) provided the first resolved measurements of the inner disk using VLTI/GRAVITY observations, which they used to investigate the mutual alignments of the inner and outer disk components. They found that the K-band complex visibilities of their data were best fit by an inner disk model with an inclination of $i_{\rm d,inn} = 23\overset{\circ}{.}76 \pm 3\overset{\circ}{.}18$ and a longitude of ascending node of $\Omega_{\rm d,inn} = 15\overset{\circ}{.}44 \pm 7\overset{\circ}{.}44$. Refitting ALMA CO data to derive outer disk geometry, they found an outer disk inclination of $i_{\rm d,out} = 38\overset{\circ}{.}21 \pm 1\overset{\circ}{.}38$ and a longitude of ascending node of $\Omega_{\rm d,out} = 162.72.44 \pm 1\overset{\circ}{.}38$. From these measurements, they inferred that the inner and outer disks of HD142527 are statistically significantly misaligned by 59°. This difference in inclination is consistent with the inner disk generating the shadows observed in scattered light and is suggestive of dynamical disruption, namely a companion on an inclined orbit (Facchini et al. 2018).

In 2012, a companion candidate to HD 142527 A was detected with the VLT/NACO instrument (Lenzen et al. 2003; Rousset et al. 2003) using Sparse Aperture Masking (SAM) at 88 mas separation, with an estimated mass of $0.1 - 0.4\,M_\odot$ (Biller et al. 2012). Subsequently, the Magellan Adaptive Optics (MagAO) team used the Visible Light Adaptive Optics (VisAO) instrument to confirm the companion by directly imaging HD 142527 B in Hα ($\Delta\mathrm{mag} = 6.33 \pm 0.20$ mag) and in 643 nm continuum ($\Delta\mathrm{mag} = 7.50 \pm 0.25$ mag) with a combination of Angular Differential Imaging (cADI) and S-SDI (referred to hereafter as ASDI; Close et al. 2014a). The presence of Hα excess in the VisAO detection indicated that the companion was actively accreting at a rate of $\sim\dot{M} = 5.9 \times 10^{-10}\,M_\odot\,\mathrm{yr}^{-1}$ (Close et al. 2014a).

The companion was also imaged using the Gemini Planet Imager (GPI; Macintosh et al. 2014) in total intensity at Y-band with Angular Differential Imaging (ADI)/Principal Component Analysis (PCA) and polarized intensity light with Polarized Differential Imaging (PDI) and ADI/PCA (Rodigas et al. 2014). Interestingly, the polarized light detection was marginally spatially inconsistent with the total intensity source by $\sim$20 mas at 2σ confidence in their reduction, which they interpret either as scattered light from the disk around the companion, or a clump of dust separated from the companion.[11]

The companion was subsequently characterized using VLT/NACO and Gemini/GPI SAM; it was confirmed to exhibit infrared excess indicative of a 1700 K circumsecondary environment and was found to be significantly younger (1.0 ± 1 Myr) than A (Lacour et al. 2016). Lacour et al. (2016) fit a mass of $M_{\rm B} = 0.13 \pm 0.03\,M_\odot$ and a temperature of $T_{\rm B} = 3000 \pm 100$K to the SED of the object. Using the SPHERE/SINFONI instrument (Eisenhauer et al. 2003), Christiaens et al. (2018) find $T_{\rm B} = 3500 \pm 100$ K, a spectral type of M2.5, and therefore an age of $0.75 \pm 0.25 Myr$ and mass of $M_{\rm B} = 0.35\,M_\odot$ with a recovered spectrum that is significantly brighter than that found in Lacour et al. (2016). They do not investigate this discrepancy.[12]

The SPHERE IFS and IRDIS instruments were used to examine the companion via NIR direct imaging and SAM (Claudi et al. 2019). Their results suggest best-fit temperatures in the range of 2600–2800 K, closer to those fit in Lacour et al. (2016), and a spectral type M5-6. They also demonstrate variability in the differential flux of B with respect to the brightness of A on the order of half a magnitude between 1–1.6μm. While this could be due to the variability of the primary star, Claudi et al. (2019) quantified the variability of the primary and found it was insufficient to explain the variability in the continuum flux of HD 142527 B. They place dynamical constraints on the mass of HD 142527 B, finding $M_{\rm B} = 0.26^{+0.16}_{-0.14}\,M_\odot$.

Cugno et al. (2019) observed HD 142527 B using SPHERE/ZIMPOL in Hα with ADI+S-SDI in a fashion similar to that of Close et al. (2014a). They recovered the companion in three filters—a broad Hα filter, a narrow Hα filter, and a continuum filter. They confirmed Hα excess emission from the companion and estimated an accretion rate of $\sim\dot{M} = 1$–$2 \times 10^{-10}\,M_\odot\,\mathrm{yr}^{-1}$, marginally lower than that derived by Close et al. (2014a).

Further study of HD 142527 B informs a number of open questions in the fields of star and planet formation. The extreme mass ratio ($\sim$20: 1) between the primary and secondary in this system, the fact that HD 142527 B is orbiting within a transition disk cavity, and its ongoing accretion make the system a higher-mass analog to protoplanetary systems such as PDS 70 b&c, allowing for the refinement of techniques used to image these systems in visible light.

The HD 1425257 system itself is also an important probe of the processes of planet formation in binary systems. Improved

[11] It should be noted that Avenhaus et al. (2017) do not detect a compact polarized source in their SPHERE/ZIMPOL images of the circumprimary environment.

[12] This may be due to a distance scaling error; see discussion in Greenbaum et al. (2019).

orbital constraints can place limits on the mutual inclinations between the HD 142527 AB binary orbit and the inner and outer disk segments (Czekala et al. 2019). Recent VLTI/GRAVITY observations of the inner disk are especially important to consider, as it is likely that HD 142527 B is responsible for the inclination of the misaligned inner disk. Orbit fits to the HD 142527 binary allow mutual inclinations of all three components of the system (the inner disk, binary, and outer disk) to be determined and compared to hydrodynamical models.

The nature of the HD 142527 B companion itself is also broadly informative of star and planet formation processes, as its young age relative to HD 142527 A might indicate that it formed from the disk via disk instability. It could also be that HD 142527 B formed at the lower end of the IMF, was dynamically captured, and is disrupting planet formation around HD 142527 A. In either scenario, its motion necessarily drives the dynamical evolution of the disk (e.g., Aly et al. 2021).

Observations of the companion to date have only covered a 60°–70° orbital arc. The nature of HD 142527 B's orbit and its relationship to both the wide observed cavity in the circumbinary disk and the inner circumprimary disk are still areas of ongoing study that can be improved by further constraining the orbital elements, in particular the eccentricity and inclination of the binary orbit and the mutual inclinations of the various components. Until the orbit is very well-characterized, it cannot be certain whether the companion can be held solely responsible for the massive cavity.

Additionally, relatively little is known about the density and dynamics of gas flow through transitional disk cavities or the reprocessing of material in circumsecondary accretion disks. Accretion rates and epoch-to-epoch variations in accretion rate can inform accretion processes for companions in these actively planet-forming systems.

In this work, we build upon previous detections of Hα excess emission from HD 142527 B. We monitor the companion's astrometric motion in visible light and provide the most complete orbital solution to date, enabling a more precise comparison between the mutual inclinations of system components. We leverage additional epochs of observation at Hα in order to argue that the accretion onto the companion is likely variable on (at least) yearly timescales.

3. Observations and Data Reduction

3.1. VisAO Observations

We observed HD 142527 with the Magellan Adaptive Optics (Close et al. 2013; Morzinski et al. 2016) VisAO (Males et al. 2014) instrument in Hα SDI mode (Close et al. 2014b) on seven nights between 2013 and 2018. Table 1 records general information about the VisAO observations of HD 142527. During observations, the telescope rotator was turned off, resulting in rotation of the FOV, which enables ADI. More field rotation allows for more reference images to be used in constructing the PSF model, improving its quality; this is especially important for tightly separated companions like HD 142527 B. The total field rotation for each observation is noted in Table 1. HD 142527 A was dithered across the CCD throughout the observing night, to mitigate the effects of near-focus dust spots in the images. MagAO uses a Natural Guide Star (NGS) to conduct wave front corrections, and in all data sets the NGS used was the on-axis science target, HD 142527 A. The SDI observing mode splits the incoming light using a Wollaston beam splitter, and this results in simultaneous continuum ($\lambda_c = 656$ nm, $\Delta\lambda = 6.32$ nm) and Hα ($\lambda_c = 643$ nm, $\Delta\lambda = 6.20$ nm) images (512×1024 pixels in size) on the top and bottom of the CCD, respectively.

We conducted a revised calibration of the absolute astrometric solution for the VisAO instrument, which is documented in detail in Appendix A. We determined an updated platescale and North Angle offset by tying observations of the θ^1 Ori B multiple system over 6 yr to observations of the same system taken over 20 yr with the precisely astrometrically calibrated Keck/NIRC2 instrument (Yelda et al. 2010; Service et al. 2016). The updated VisAO platescale is 7.95 ± 0.010 mas pix^{-1}, and the updated North Angle offset is $0\overset{\circ}{.}497 \pm 0\overset{\circ}{.}192$ counterclockwise. This new solution does not necessitate a revision of previously published results, as both values agree with previous calibrations within error bars (Close et al. 2013; Males et al. 2014). However, the updated calibration improves the accuracy of VisAO astrometry, and validates the stability of the North Angle offset between instrument mountings, which occur every semester.

3.2. Preprocessing

VisAO data were reduced and preprocessed with the GAPlanetS data reduction pipeline described in detail in Follette et al. (2017) and K. B. Follette et al. (2022, in preparation). In short, images were dark-subtracted, flatfielded (except for the 2013 April 11 data set, for which no flatfields exist), split between Hα and continuum channels, and registered using a Fourier cross-correlation algorithm, which yields errors on the position of the central star of $\sim$0.1 pix (K. B. Follette et al. 2022, in preparation).

In half of our observations (three out of seven; see Table 1), the central star was allowed to saturate in order to improve the signal-to-noise ratio (S/N) in the search for additional companions within the system. A stable instrumental ghost appears in VisAO images to the right of the natural guide star (NGS). We investigated the stability of the ghost as a photometric and astrometric calibrator for saturated data, and found it to be suitable for both purposes (see Appendix B).

Following alignment, images with cosmic rays within 50pix ($\approx 0\overset{''}{.}04$) of the central star were rejected by hand. Images were then cropped to a 451 pixel ($\sim 3\overset{''}{.}5$) square surrounding the central star.

We then measured the "Hα scale factor" by conducting aperture photometry on the central star (or ghost, for saturated images) for each image in the sequence. We adopt the median of the ratios between the Hα flux and the continuum flux for each image in the sequence as the best estimate of the scale factor ($F_{*,\mathrm{H}\alpha}/F_{*,\mathrm{Cont}}$), and the standard deviation as the uncertainty, and these values are recorded in Table 1. This scale factor is an estimate of the Hα excess of the primary star, and allows us to quantify the accretion variability of the host star itself and to correct for the effect of stellar accretion on measured contrasts for the companion (see Section 5).

3.3. PSF Subtraction

We conducted PSF subtraction using the Python implementation of Karhunen–Loeve Image Processing, `pyklip`[13] (Wang et al. 2015). The `pyklip` input parameters

[13] https://pyklip.readthedocs.io

Table 1
VisAO Observations of HD 142527

Date (YY/MM/DD)	N_{ims}	Exposure (s)	Total integration (m)	Total rotation (°)	FWHM (mas)	Saturation radius (pix)	Avg. Seeing (″)	Stellar Hα/Cont.
2013-04-11	1961	2.27	74.2	65.3	25.0	⋯	⋯	0.83 ± 0.03
2014-04-08	1758	2.27	66.5	101.7	38.9	⋯	⋯	1.11 ± 0.10
2015-05-15	2387	2.27	90.3	117.4	37.8	⋯	0.55	1.19 ± 0.23
2015-05-16	1143	2.27	43.2	34.8	33.8	2	0.80	1.17 ± 0.07
2015-05-18	159	30	79.5	76.8	30.7	9	0.66	1.16 ± 0.08
2017-02-02	242	12	48.4	16.1	43.7	2	0.72	1.13 ± 0.02
2018-04-27	580	5	48.3	49.2	28.5	3	⋯	1.31 ± 0.10

Notes. The average seeing was determined by measurements taken from the DIMM, Magellan Baade, or both (in which case, the two are averaged). For data sets where no external seeing information exists, the column is left blank. The stellar Hα/ Cont. ratios are calculated by performing aperture photometry on every image in both wavelengths for each data set. We extract photometry from the central star in the case of unsaturated data sets, and from the instrumental ghost in the case of saturated data. We report the median ratio for each data set in the table above. A ratio < 1 indicates a relatively quiescent phase in the accretion onto the primary.

`movement`, `annuli`, and `numbasis` were chosen based on the optimization techniques described in J. Adams Redai et al. (2022, in preparation) as developed for the the Giant Accreting Protoplanets Survey (K. B. Follette et al. 2022, in preparation). In brief, the `pyklip` `movement` parameter is an exclusion parameter that removes images from the reference library in which a companion at a given separation from the star would have shifted (rotated with the sky) by fewer than the specified number of pixels relative to the image for which the PSF model is being constructed. The `annuli` parameter describes the size of annular zones that `pyklip` treats separately, where the width of the annulus is $\Delta r = (\mathrm{OWA} - \mathrm{IWA})/\mathrm{annuli}$. Generically, the inner edge of each annulus is defined as $r_{\mathrm{in}} = \mathrm{IWA} + \Delta r \times n$, but for HD 142527 B, the companion always lies within the inner annulus, so $n = 1$ and $r_{\mathrm{in}} = \mathrm{IWA}$, while $r_{\mathrm{out}} = \mathrm{IWA} + \Delta r$. Our images are non-coronagraphic, so they do not have a hardware-determined inner working angle. However, we found that applying one in software generally improves our detections, and we have adopted a fixed value of $1 \times \mathrm{FWHM}$ here. The `numbasis` parameter controls the number of principal components, or KL modes, included in the constructed PSF. We chose to fix the maximum number of KL basis vectors used to construct the PSF at 100 and applied a pre-KLIP high pass filter of $1 \times \mathrm{FWHM}$ in all analyses, to match the broader GAPlanetS Survey strategy.

We refer the reader to J. Adams Redai et al. (2022, in preparation) for additional information on the optimization of `pyklip` parameters for GAPlanetS data. To briefly summarize the optimization method used here, we:

1. conduct a grid search in `pyKLIP`'s `movement`, `annuli`, and `numbasis` (KL mode) parameters and generate KLIP images for each combination.
2. compute six "image quality metrics" for each `movement`, `annuli`, and `numbasis` combination. These metrics are: peak S/N of the companion(s), average S/N of the companion(s), the "neighbor quality" of the previous two metrics (computed by smoothing their metric maps), false-positive ($>5\sigma$) pixels, and contrast, normalized so that their best (highest for S/Ns, lowest for contrast and false-positive pixels) values are equal to unity.
3. Sum or average across a desired choice of metrics, companion(s), and KL modes, to select "optimal" values for each of the three KLIP parameters.

For this work, the targets of the optimizations for most data sets were "false planets" inserted into the continuum images. In these data sets, we optimized on the sum of all six normalized image quality metrics averaged between five and 20 KL modes and across four to eight false planets (as many as would fit with a radial spacing of $0.5 \times \mathrm{FWHM}$ and an azimuthal spacing of 85^o between the IWA and control radius of each data set) in order to select the optimal `movement` and `annuli` parameters. We then selected a single optimal `numbasis` value by maximizing the sum of the six normalized metrics for the optimal combination of `annuli` and `movement`. The optimal values for all three parameters are reported in Table 2.

Table 2
Adopted `pyklip` Starlight Subtraction Parameters

Date	Movement	Annuli	KL mode
2013-04-11	1	14	20
2014-04-08	1	25	100
2015-05-15	2	20	20
2015-05-16	12	1	12
2015-05-18	7	2	5
2018-04-27	1	25	20

Although the companion is recovered in all epochs using this parameter selection method, which optimizes for robust recovery of companions throughout the region between the IWA and control radius, it is not necessarily the best choice of parameters for the specific location of the companion. In the case of a robust known companion like HD 1425257 B, optimization can also be done on the location of the companion itself in Hα images, and we utilize this method to achieve higher S/N recoveries of the companion in the 2015 May 16 and 2018 April 27 data sets. For these epochs, we optimize on the sum of the peak and average S/N metrics for the companion, and select the `annuli`, `movement`, and `numbasis` parameters that maximize this sum. Since each epoch of VisAO data for HD 142527 B has a corresponding near-in-time NIR detection, we optimized the KLIP parameters on the known NIR location of the companion. Contrast curves and limits on additional companions in the HD 142527 cavity appear in the upcoming GAPlanetS survey paper, K. B. Follette et al. (2022, in preparation).

4. Results

Using `pyklip`, we detect the companion in both filters in all epochs of observation except 2017 February 02, where the total field rotation was too small ($16.^\circ1$) to achieve the necessary

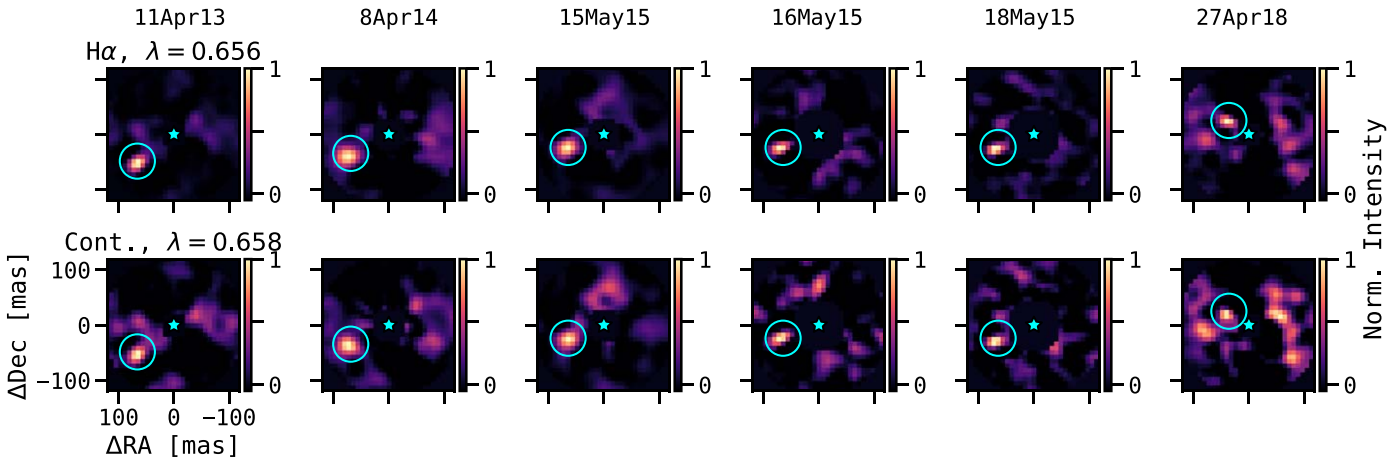

Figure 1. Gallery of post-KLIP images showing the detections of HD 142527 B in Hα (top) and continuum (bottom). The colorbar is normalized to the peak pixel value of the companion in each image. The cyan circle indicates the nearest in time position of HD 142527 B reported in previous literature (Lacour et al. 2016; Claudi et al. 2019). The cyan star indicates the position of HD 142527 A. The innermost pixels have been masked to $r \sim 1$ FWHM for each data set.

contrast to detect the very tightly separated companion.[14] As expected, the observations with the greatest total field rotation (2015 May 15) and best atmospheric quality (2013 April 11) yielded the highest S/N recoveries of the companion. Figure 1 shows each recovery in Hα and continuum. We quantify the quality of each recovery using the forward modeling capabilities of `pyKLIP`.

4.1. Bayesian Forward Modeling

To determine the astrometry of the imaged companion, we implement KLIP forward modeling (Pueyo 2016) and conduct Bayesian Klip Astrometry (BKA; Wang et al. 2016). This technique involves the projection of a companion PSF estimate onto the basis vectors used to construct the primary KLIP PSF model to synthesize a forward-modeled PSF. This forward model is fit to the post-KLIP data using an affine-invariant MCMC with `emcee` (Foreman-Mackey et al. 2013). This produces a posterior distribution of model fits that yields robust uncertainties on astrometry and photometry. We take the median of the posterior distribution of a given parameter as its measured value and the 16th and 84th percentiles as uncertainties on that median. The strength of KLIP forward modeling when compared to negative planet injection grid searches is the speed and precision of model fitting and convergence, which enables the application of a Bayesian analysis framework as well as the capability to model correlated noise within the images using a Gaussian process.

For unsaturated data, we find that using a 2D Gaussian PSF with the FWHM of the median stellar PSF produces excellent forward model fits (see discussion in Appendix B).

For saturated data sets, we do not have a direct measure of the stellar FWHM. In Appendix B, we investigate the suitability of a range of forward models in extracting astrometry and photometry for the tight HD42527B companion in saturated data sets. In short, we find that the ghost is suitable as a photometric calibrator (see Appendix B), and determine that the ratio of the peak value of a Moffat fit to the ghost to the peak value of a Moffat fit to the unsaturated NGS PSF in unsaturated data is a stable quantity. We also find that the ghost is slightly out of focus, and that its FWHM is ∼7% wider than the stellar FWHM in unsaturated data sets. This result matches our expectations: as the ghost is produced by a reflection off of the MagAO 50/50 beam splitter, it has a longer path than the zeroth-order source, and is therefore slightly out of focus. We assume that both the star-to-ghost brightness scaling and the FWHM discrepancy hold in the case where the NGS is saturated, and estimate the FWHM of our saturated data sets by taking $0.93 \times \mathrm{FWHM}_{\mathrm{ghost}}$. We find that the optimal forward model for saturated data is a Gaussian PSF whose FWHM was set to the $0.93 \times \mathrm{FWHM}_{\mathrm{ghost}}$ in order to match the expected FWHM of the image plane PSF.

In order to further quantify the strength of our detections, we utilize the `PlanetEvidence` class (Golomb et al. 2019) within `pyklip` to conduct a Bayesian model comparison and determine the S/N of HD 142527 B for a given detection. `PlanetEvidence` uses the nested sampling implementation `pyMultiNest` (Feroz et al. 2009; Buchner et al. 2014) to compare two models: H_0, where the image contains only speckle noise, and H_1, where the image contains a source at the position of HD 142527 B. `PlanetEvidence` returns marginal distributions of the parameters for the source and null cases, and calculates the S/N of the detection within the fitting region and the evidence values for H_0 and H_1 (Z_0 and Z_1). The log-ratio of these evidence values, $\log B_{10} = \log Z_1/Z_0$, enables us to quantify the confidence with which one model can be favored over the other.[15] This framework provides a more robust estimate of the quality of the detection, better capturing asymmetric speckle noise that can dominate at very close separations than S/N computed within an annulus. The S/N values reported in Table 4 are calculated from the residuals within the fitting region as described in Golomb et al. (2019).

For example, values for $\log B_{10} > 5$ are considered "strong" evidence against the null hypothesis. We achieved strong evidence ($\log B_{10} > 10$) in all cases, and unambiguous detections ($\log B_{10} > 20$) in 11 out of 12 data sets. While the evidence is not strong for the detection in the continuum for the 2018 April 27 epoch, the search for the companion in this

[14] At the expected separation in this epoch (50 mas; Claudi et al. 2019), the highest contrast observable within this data set was 0.5×10^{-2}, whereas our *brightest* detection of HD 142527 B across all epochs was at a contrast of 0.3×10^{-2}.

[15] See Golomb et al. (2019) for definitions of the evidence values, discussion of log-ratios, and an example involving quantifying the detection of β Pictoris b.

Table 3
Results of Forward Model Fitting and Companion S/N

Date (DD/MM/YY)	Separation (mas)	PA (°)	Δmag (mag)	$\log Z_1/Z_0$	S/N
Continuum					
2013-04-11	82.74 ± 1.51	128.07 ± 0.68	7.3 ± 0.2	75.89	5.24
2014-04-08	78.25 ± 3.39	116.00 ± 2.45	7.2 ± 0.3	22.33	5.82
2015-05-15	70.63 ± 1.95	112.28 ± 1.38	7.4 ± 0.2	22.77	7.85
2015-05-16	70.59 ± 4.36	107.33 ± 2.10	7.4 ± 0.3	37.14	5.37
2015-05-18	73.70 ± 3.92	110.97 ± 2.24	7.3 ± 0.3	77.43	5.98
2018-04-27	42.75 ± 3.22	58.53 ± 2.95	7.3 ± 0.4	13.55	2.64
Hα					
2013-04-11	82.30 ± 1.36	127.91 ± 0.61	6.29 ± 0.13	266.30	10.53
2014-04-08	77.57 ± 1.86	118.21 ± 1.04	6.59 ± 0.17	32.67	8.02
2015-05-15	69.89 ± 1.50	109.68 ± 0.98	6.88 ± 0.16	51.26	12.03
2015-05-16	72.64 ± 2.29	107.98 ± 1.09	6.73 ± 0.19	75.94	8.11
2015-05-18	69.96 ± 1.36	110.02 ± 0.76	7.11 ± 0.16	131.84	7.90
2018-04-27	44.29 ± 2.57	58.14 ± 2.20	6.9 ± 0.3	24.31	3.47

epoch is not a "blind search." We can be reasonably certain that signal at this location is due to the real companion, thanks to the near-in-time observations in the NIR (Claudi et al. 2019). Nevertheless, the continuum detection in 2018 should be approached with some skepticism.

4.2. Forward Model Results

Our Bayesian forward modeling returns posterior distributions of the x and y positions (in pixels) of the fit model, a flux scaling parameter α, and a length scale l of correlated noise within the image. We transform α into contrast by multiplying it by a constant 10^{-2} (a `pyklip` input term setting the initial contrast of the forward model) and by the peak count of the forward model (which in our case is unity, as the PSF model is normalized before it is passed to `pyklip`).

We calculate the astrometry given in Table 3 by applying the updated platescale and north angle offset (described in detail in Appendix A) to the separation and position angle measurements of the companion from the posterior distributions of forward model fits. We propagate 0.1 pix uncertainties on the position of the host star from the image registration process, 1σ uncertainties on the position of the companion from the posterior distribution of forward model fits, and estimated uncertainties on our absolute astrometry (see Appendix A for details) into our calculations to obtain final uncertainty estimates on separation and PA measurements for the companion.

We determine the Hα contrast of the companion relative to the primary star reported in Table 3 as follows. First, we take the median and standard deviation on the forward model fit to the contrast (C_{B-A}) as the derived value and uncertainty, respectively. For the continuum filter, this value can be converted to a contrast in magnitudes via a simple magnitude transformation, namely $\Delta\mathrm{mag} = -2.5\log C_{B-A}$. However, at Hα, the star itself is actively accreting, influencing the Hα contrast extracted from BKA. In order to measure the Hα contrast of the companion *with respect to the stellar continuum*, we multiply the BKA-derived contrast of the companion at Hα ($F_{\mathrm{comp,H}\alpha}/F_{*,H\alpha}$) by the stellar Hα to continuum scale factor for the observations ($F_{*,\mathrm{H}\alpha}/F_{*,\mathrm{Cont}}$, determined as described in Section 3 and given in Table 1). This leaves us with the contrast of the companion at Hα *relative to the stellar continuum* ($F_{\mathrm{comp,H}\alpha}/F_{*,Cont}$) and allows us to compare the brightness of the companion at Hα over time without being influenced by stellar Hα variability. We propagate errors on the BKA-derived contrast and scale factor through the logarithmic transformation to magnitude.

Table 3 records the results of our forward model fits to the astrometry and photometry of continuum and Hα images for each epoch. Figure 2 illustrates a representative model fit and residuals for the 2013 April 11 data set, and galleries of forward model fits to other epochs can be found in Appendix C.

5. Analysis and Discussion

We calculate the separation and PA of the companion on each night of observation as the weighted mean of the x and y positions in the Hα and continuum filters, where the weights are the uncertainties in each filter (calculated as described in Section 4). The final uncertainty on the Hα and continuum averaged position is then the square root of the sum of the uncertainties on the individual measurements. Table 4 records the final VisAO astrometry together with previous astrometry from the literature, and these positions are plotted in Figure 3.

5.1. Orbit Fitting

By combining our derived astrometry with compiled results from the literature, we compute orbits fit to the motion of HD 142527 B with `orbitize!` (Blunt et al. 2020), an open-source Python package that performs Bayesian orbit fitting for directly imaged companions.[16] We use the parallel tempered (Vousden et al. 2016) affine-invariant (Foreman-Mackey et al. 2013) MCMC sampler in `orbitize!`, in order to determine the posterior probabilities for eight orbital parameters: semimajor axis (a), eccentricity (e), inclination angle (i), argument of periastron of the companion's orbit (ω), longitude

[16] https://orbitize.info

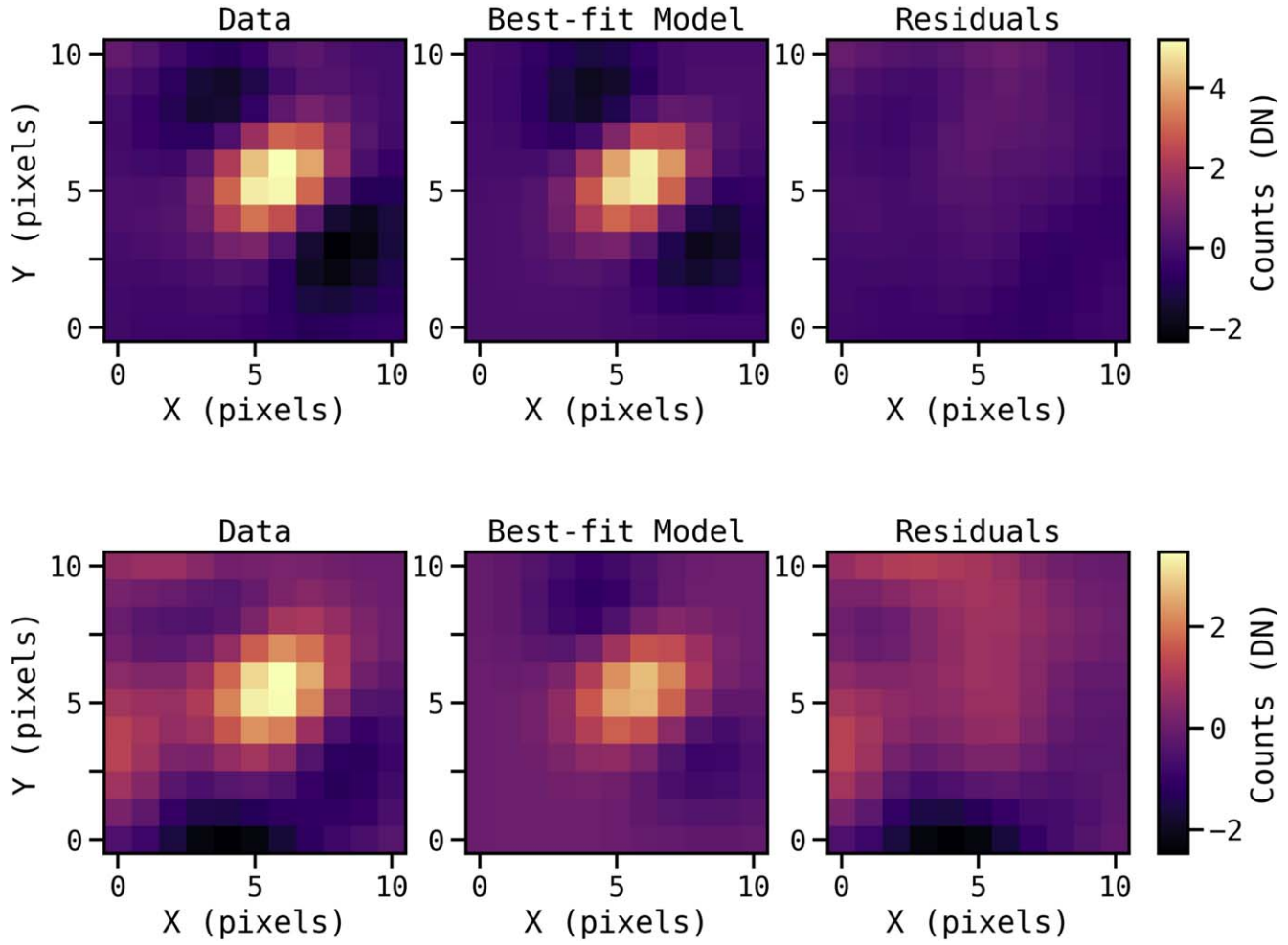

Figure 2. Representative `pyklip` forward model fits for HD 142527 B. Shown are the 2013 April 11 Hα (top row) and continuum (bottom row) detections. Based on the `PlanetEvidence` analysis, the evidence ratios $\log Z_1/Z_0$ are 266.30 and 75.89 in Hα and continuum, respectively. Both are considered extremely strong evidence in favor of the existence of the companion at this location.

of ascending node (Ω), epoch of periastron passage (τ), system parallax (π), and total mass of the binary system ($M_{\rm tot}$).

We assume default `orbitize!` priors except on the total mass of the system and the system parallax. We set a Gaussian prior on the system parallax, $\mathcal{N}(\mu = 6.356, \sigma = 0.047)$, following the measured Gaia eDR3 parallax (Gaia Collaboration et al. 2021). We adopt a Gaussian prior on the total system mass ($M_{\rm tot}$) of $\mathcal{N}(\mu = 2.3\,M_\odot, \sigma = 0.3\,M_\odot)$ based on the results of Mendigutía et al. (2014) and Claudi et al. (2019). We refer the reader to Blunt et al. (2020) for information about `orbitize!` default priors, as well as more detailed descriptions of the variables involved in the orbital solution. Posterior distributions are computed by first initializing an MCMC with 50 walkers and 20 temperatures for a 100,000 step burn-in phase per walker; the walker samples are discarded before a total of 5,000,000 additional samples are recorded to approximate the posterior.

Table 5 records our estimates of the orbital elements for HD 142527 B. Figure 4 shows 100 randomly drawn orbits from our posterior distribution of orbit fits overplotted on the astrometry compiled in Table 4. The full corner plot visualizing the posterior distributions of all eight orbital parameters (Figure 14) can be found in Appendix D. Our additional VisAO astrometry provides marginally tighter constraints relative to previous orbital solutions. We note, however, that our MCMC approach is likely more robust under poorly constrained posterior distributions than previous Least Squares Monte Carlo approaches (see discussion in Section 2.3.2 of Blunt et al. 2020).

Our `orbitize!` orbit fitting yields well-converged unimodal distributions in all parameters except ω and Ω, which show bimodal distributions with peaks spaced 180° apart. This known degeneracy in visual orbits with a lack of RV constraints.[17] To avoid confusion, we report values of the first (0°–180°) modes of ω and Ω in Table 5, noting that solutions with values 180° higher are equally likely.

Previous orbital solutions to the motion of HD 142527 B have have shown it to be both inclined ($i \sim 125° \pm 5°$ Lacour et al. 2016) and eccentric ($e > 0.2$ Lacour et al. 2016; Claudi et al. 2019). Our unimodal eccentricity distribution ($e = 0.24 \pm 0.15$) agrees with the first family of eccentricities fit by Claudi et al. (2019) ($e \sim 0.2 - 0.45$); we do not reproduce their additional family of eccentricities ($e \sim 0.45$–0.7). This could be due to the increased weight our additional astrometry

[17] HD 142527 A is a pre-main-sequence F type star, which makes RV measurements particularly challenging. RV measurements for the system have been included in large pipeline surveys, such as the HARPS-RVBANK, but we choose not to consider these RVs for our orbital fitting, because they are likely dominated by stellar jitter, which is outside of the scope of this paper to treat properly.

Table 4
HD 142527 B Astrometry

Date (DD/MM/YY)	Separation (mas)	Position Angle (°)	Instrument	Source
2012/3/11	89.70 ± 2.60	133.10 ± 1.90	NACO	B12
2013/3/17	82.00 ± 2.10	126.30 ± 1.60	NACO	L16
2013/4/11	82.50 ± 1.01	127.98 ± 0.46	VisAO	This work
2013/7/14	82.50 ± 1.10	123.80 ± 1.20	NACO	L16
2014/4/8	77.73 ± 1.63	117.87 ± 0.96	VisAO	This work
2014/4/25	88.10 ± 10.10	123.00 ± 9.20	GPI	R14
2014/5/10	78.00 ± 1.80	119.10 ± 1.00	SINFONI	Ch18
2014/5/12	77.20 ± 0.60	116.60 ± 0.50	GPI	L16
2015/5/13	69.00 ± 2.00	110.20 ± 0.50	IFS/IRDIS	Cl19
2015/5/15	70.16 ± 1.19	110.56 ± 0.80	VisAO	This work
2015/5/16	72.19 ± 2.02	107.84 ± 0.97	VisAO	This work
2015/5/18	70.00 ± 1.35	110.12 ± 0.72	VisAO	This work
2015/7/3	65.50 ± 0.40	106.20 ± 0.40	IFS/IRDIS	Cl19
2016/3/26	60.00 ± 2.00	97.10 ± 0.50	IFS/IRDIS	Cl19
2016/3/31	62.80 ± 2.70	98.70 ± 1.80	ZIMPOL	Cu19
2016/6/13	61.00 ± 2.00	96.30 ± 0.50	IFS/IRDIS	Cl19
2017/5/16	48.50 ± 0.50	77.80 ± 0.20	IFS/IRDIS	Cl19
2018/4/14	44.00 ± 1.00	55.40 ± 0.40	IFS/IRDIS	Cl19
2018/4/27	43.69 ± 2.01	58.28 ± 1.76	VisAO	This work

Note. Sources for the listed astrometry in order of appearance are B12 = Biller et al., L16 = Lacour et al., R14 = Rodigas et al., Ch18 = Christiaens et al., Cl19 = Claudi et al., and Cu19 = Cugno et al.

places on the position of the companion in 2018, or due to differences in the exploration of parameter space between the LSMC and MCMC frameworks. We further constrain the system inclination to $i = 126° \pm 2°$.

The longitude of ascending node (Ω) and time of periastron passage of an orbit are more difficult to constrain with limited azimuthal coverage. Claudi et al. (2019) placed constraints of 124°–135° and 2020–2022 on these values. Our value of time of periastron passage, $2021.07^{+0.82}_{-0.72}$ agrees with their estimate within error bars, but our refined $\Omega = 142.38^{+5.51}_{-6.12}$ marginally disagrees; our solutions preferring a somewhat higher value. According to our orbital fits, periastron passage has likely already occurred for HD 142527 B.

HD 142527 B's orbit is interesting in the context of star and planet formation, in that its eccentricity might indicate a stellar formation history. Directly imaged brown dwarf companions have been found to have a distribution of eccentricities that favor higher values when compared to directly imaged planets (Bowler et al. 2020), suggesting that they form independent of the system and are captured, rather than arising from within the circumplanetary disk. HD 142527 may therefore be more analogous to objects like GQ Lup B (Wu et al. 2017; Stolker et al. 2021), a captured, accreting, very low-mass object that is dynamically truncating/disrupting its circumprimary environment, than to accreting protoplanets.

5.2. Mutual Inclinations

In order to contextualize our results within the broader HD142527 system architecture, Figure 5 superimposes (a) 50 randomly drawn orbits from the posterior distribution of orbit fits, (b) a single-epoch VisAO detection of the Hα point source, and (c) an H-band polarized intensity observation of the HD142527 outer disk. The image of the circumbinary disk was

Table 5
HD 142572B Orbital Elements

Element	Value
a (au)	$14.71^{+8.18}_{-2.33}$
e	$0.28^{+0.22}_{-0.10}$
i (°)	$126.27^{+2.13}_{-2.28}$
ω(°)	$86.02^{+52.31}_{-42.59}$
Ω(°)	$142.38^{+5.51}_{-6.12}$
Time of periastron passage (yr)	$2021.07^{+0.82}_{-0.72}$
$M_{\rm total}(M_\odot)$	$2.49^{+0.27}_{-0.27}$
Parallax (mas)	6.36 ± 0.05
$\theta_{\rm in-\star}$(°)	$56.55^{+2.93}_{-2.79}$, $66.38^{+1.84}_{-1.36}$
$\theta_{\star-\rm out}$(°)	$45.87^{+2.05}_{-1.53}$, $76.49^{+2.66}_{-2.72}$

obtained by re-reducing GPI polarimetric data first published in Rodigas et al. (2014) using the updated GPI DRP described in De Rosa et al. (2020); these data were then interpolated to VisAO's platescale in order to facilitate comparison with VisAO observations of the companion (shown for all epochs in Figure 1).

The "mutual inclination" between the orbit of a binary star and its circumbinary disk is expected to inform the evolution of the circumbinary and circumstellar environments, and has wide-ranging implications for planet formation in binary systems (Czekala et al. 2019). While external binary companions may significantly truncate a circumstellar disk, perhaps suppressing planet occurrence (Kraus et al. 2016), circumbinary disks around tighter binary systems result in circumbinary planets (e.g., Kostov et al. 2020, 2021). The HD 142527 system is interesting to consider in this context because it is one of a handful of systems with direct imaging measurements of both the inner and outer disk components as well as the binary orbit.

The mutual inclination between the disk plane and binary orbit, θ, is defined as

$$\cos\theta = \cos i_{\rm d}\cos i_\star + \sin i_{\rm d}\sin i_\star\cos(\Omega_{\rm d} - \Omega_\star),$$

where θ is the angle between the angular momentum vector of the binary orbit and the midplane of the disk (Czekala et al. 2019).

We determine the posterior distribution of mutual inclinations between the binary orbit and both the inner and outer disk components (shown in Figure 15) by drawing random samples from the posterior distribution of $i_\star$ and $\Omega_\star$ produced by `orbitize!`, and assuming a Gaussian distribution for the disk orientation centered on the values most recently inferred from ALMA gas kinematic data for the outer disk ($i_{\rm disk,outer} = 38.^\circ21 \pm 1.^\circ38$, $\Omega_{\rm disk,outer} = 162.^\circ72 \pm 1.^\circ38$; Perez et al. 2015; Boehler et al. 2017; Bohn et al. 2022), and VLTI/GRAVITY observations for the inner disk ($i_{\rm disk,inner} = 23.^\circ76 \pm 3.^\circ18$, $\Omega_{\rm disk,inner} = 15.^\circ44 \pm 7.^\circ44$; Bohn et al. 2022).

Regardless of the 180° ambiguity in $\Omega_\star$, the current orbital solution for HD 142527 B yields large mutual inclinations throughout the system. We find $\theta_{\star-\rm out} = 45.87^{+2.05}_{-1.53}(^\circ)$ or $76.49^{+2.66}_{-2.72}(^\circ)$ (due to the mutual inclination's dependence on the bimodal $\Omega_\star$). These values are not consistent with those reported previously ($35° \pm 5°$) by Czekala et al. (2019), who adopted the $\Omega_\star$ solution from Claudi et al. (2019).

Our best fit to the mutual inclination of the binary with respect to the inner disk is $\theta_{\rm in-\star} = 56.55^{+2.93}_{-2.79}(^\circ)$ or $66.38^{+1.84}_{-1.36}(^\circ)$.

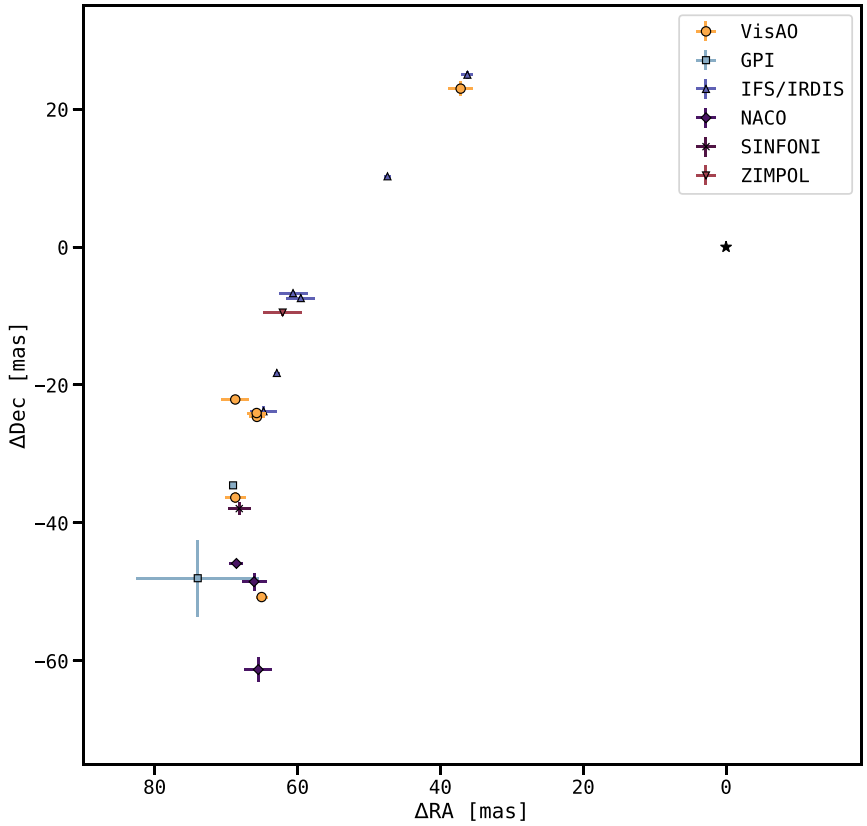

Figure 3. Astrometric measurements of HD 142527 B relative to HD 142527 A (black star) from NACO, GPI, SPHERE, SINFONI, and VisAO (this work) between 2012 and 2018. The crosses represent the reported uncertainties on each measurement. The companion experiences significant orbital motion ($\Delta\theta \approx 65°$) and decreases substantially in separation ($\Delta\rho \approx 30$ mas) from 2016 to 2018. The VisAO values (yellow circles) agree well with astrometry from other instruments. Error bars on our measurements reflect the 1–2 mas accuracy achievable using `pyklip` forward modeling.

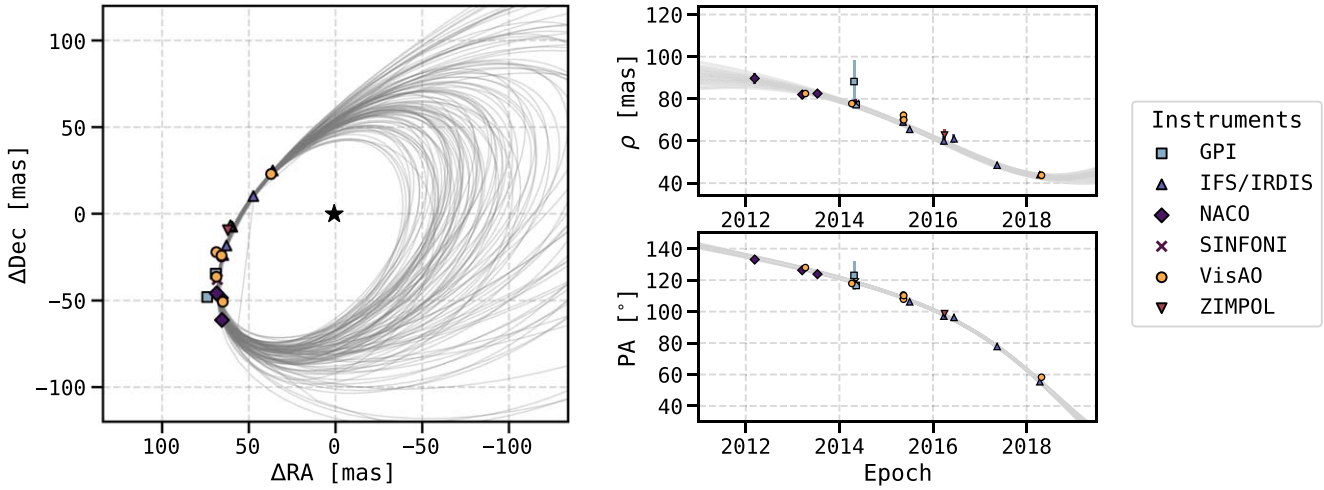

Figure 4. One hundred randomly drawn `orbitize!` orbits fit to the motion of HD 142527 B. Astrometry from Figure 3 is overplotted. Left: the orbits projected in RA and Dec, relative to HD 142527 A (black star). Right: the orbits in separation/position angle vs. time. The new VisAO astrometry does not add new coverage of the orbital arc, but the 2018 recovery adds more weight to the near-in-time SPHERE NRM astrometry.

Taken together, our mutual inclination fits present a system where each component of the system is dramatically misaligned with respect to the others.

Modeling the interaction of the binary companion and the circumbinary disk, Price et al. (2018) demonstrated that the morphological features of the circumbinary disk (wide cavity, asymmetric dust horseshoe, and spiral arms) can be qualitatively reproduced solely through interaction with the binary companion under orbits representative of those found in Lacour et al. (2016). To best reproduce the observed morphology, Price et al. (2018) favor a narrower family of eccentric orbits ($e = 0.6$–0.7) with nearly perpendicular mutual inclinations with respect to the outer disk.

Our work lends some support to this hypothesis, as one of the equal, symmetrically distributed peaks in θ (resulting from the degeneracy in $\Omega_\star$) from our orbit fits centers on

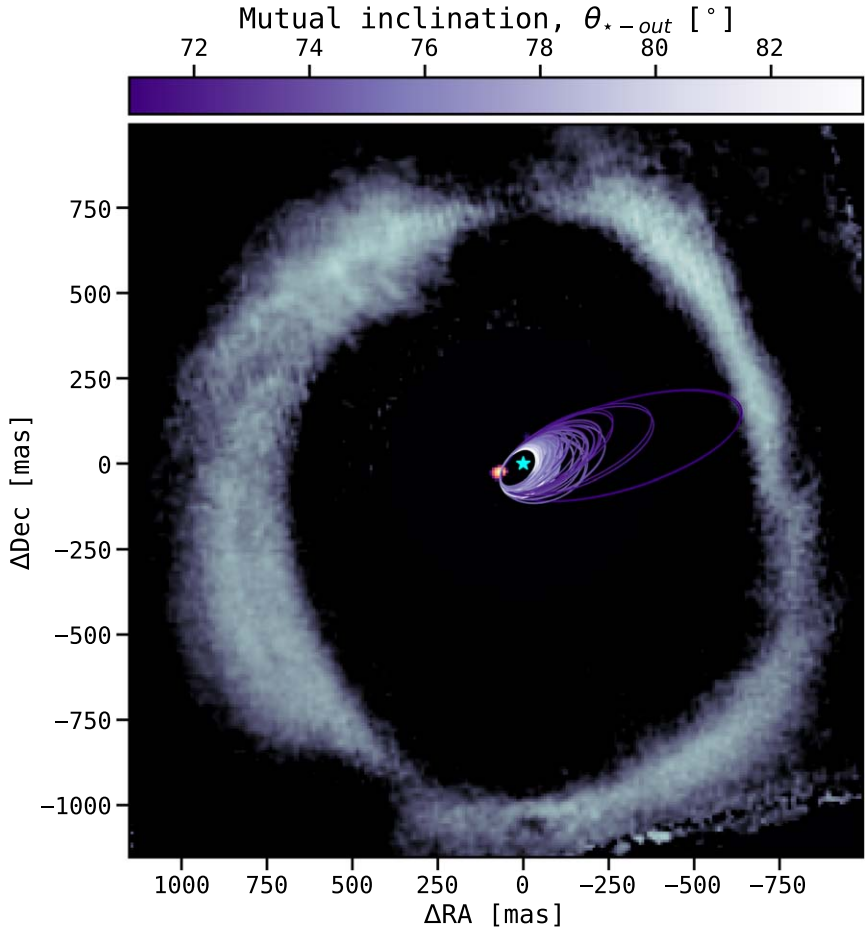

Figure 5. The orbit of HD 142527 B in context. The position of HD 142527 A is marked with a cyan star, and 250 randomly drawn orbits from fits to the astrometry of HD 142527 B are plotted with colors corresponding to their mutual inclination with the outer disk ($\theta_{\star-\mathrm{out}}$). The outer image of the circumbinary disk is a Gemini/GPI scattered light polarized intensity H-band image reprocessed with an updated GPI pipeline and interpolated to VisAO's platescale. The inner image is the post-KLIP 2015 May 15 Hα detection from VisAO (also shown in Figure 1). Both images are normalized to their respective maximum pixel values before combination.

$\theta = 79\overset{\circ}{.}93 \pm 3\overset{\circ}{.}04$, suggestive of the near-perpendicular configuration they describe. Our orbit fitting has not produced a distribution suggestive of such high eccentricities, however.

5.3. Photometry

Figure 6 plots the contrast of the companion *relative to the stellar continuum* over time, derived as described in Section 4. The Δmag measurements from Cugno et al. (2019) are overplotted to demonstrate consistency with our measurements. Between 2013 April 11 and 2015 May 15, the Hα contrast of the companion decreased by 0.68 mag. This is suggestive of a moderately variable accretion rate onto the companion on yearly timescales. Over the same baseline, the continuum did not vary within uncertainties. As there is not significant variability in the continuum contrast of the companion between epochs, this suggests that the extinction toward HD 142527 B is constant to $\pm$ 0.2 mag. Accretion-driven variability in the stellar continuum flux at our cadence is similarly limited to being at or below this value, though it likely occurs on shorter timescales (e.g., Stauffer et al. 2014).

The Close et al. (2014a) contrast measurements ($\Delta\mathrm{mag}_{\mathrm{H}\alpha} = 6.33 \pm 0.20$ mag, $\Delta\mathrm{mag}_{\mathrm{cont}} = 7.50 \pm 0.25$ mag), derived from the same data set, agree with our measurements within error bars, and we note that our slightly higher continuum brightness estimate is likely due to improved PSF subtraction and forward modeling, which allow us to better quantify flux lost to this process. While taken in marginally different filters, the Cugno et al. (2019) contrast measurements (shown with square symbols in Figure 6) agree well with our results; their continuum contrast measurement falls along our median continuum contrast and their Hα contrast lies within the range of values we have measured, with similar uncertainties.

Our method for calculating the contrast of the companion with respect to the stellar continuum should should be insensitive to stellar Hα variability, leaving only stellar continuum variability as a potential contaminant. The star has a known periodicity of $\sim$6 days, with a peak-to-valley amplitude of 0.09 mag in the R band (Claudi et al. 2019), too small to account for the observed variation in the Hα channel. If stellar continuum variability were contaminating the observed Hα variation, we would expect to see it directly in our measurements of the companion's continuum contrast, and we do not observe such variation. We note that the companion's infrared continuum has been observed to vary on the order of 0.5 mag (Claudi et al. 2019), but we do not observe a similar variability at visible wavelengths.

Our data are therefore suggestive of variability in the Hα emission of this directly imaged accreting companion, resulting in the observed time variability in the Hα excess. This

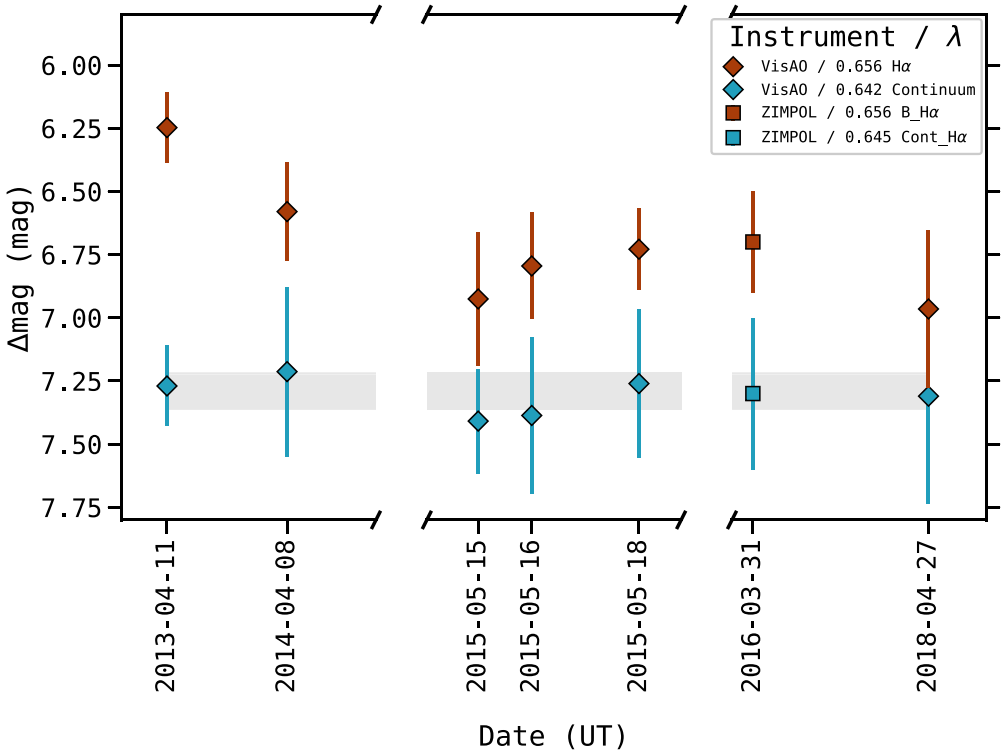

Figure 6. The visible-light contrast of HD 142527 B with respect to the continuum of HD 142527 A over time. Brown and green diamonds mark our Hα and continuum contrast measurements, respectively. The gray shaded region represents the 1σ standard deviation of our measurements of continuum contrast, centered on the median. The red and blue squares mark the contrasts measured in nearly equivalent filters by Cugno et al. (2019) using VLT/SPHERE/ZIMPOL. The amount of Hα excess appears to vary between many of the epochs, while the continuum contrast varies minimally and is consistent with uniformity within error bars.

variability has implications for future direct imaging protoplanet surveys. If accretion onto less massive companions is similarly variable, detection limits will need to be interpreted with some caution, as companions will be more quiescent at certain times.

5.4. Accretion Rate

We estimate the mass accretion rate onto HD 142527 B using Hα contrast measurements following a standard set of assumptions for accreting objects. First, we convert our contrast into a line luminosity measurement via

$$\mathrm{L_{H\alpha}} = 4\pi D^2 \times \mathrm{Z_{pt}} \times d\lambda \times 10^{((\mathrm{mag}_\star + \Delta\mathrm{mag}_B)/-2.5)},$$

where D is the distance to the system, $\mathrm{Z_{pt}} = 2.339 \times 10^{-5}\mathrm{erg\,cm^{-2}\,s^{-1}}\,\mu\mathrm{m}^{-1}$ is the Vega zero point of the Hα filter (Males et al. 2014), $d\lambda = 0.006\mu$m is the width of the Hα filter, and $\mathrm{mag}_\star = 8.1 - A_R$ is the R-band apparent magnitude of the central star (8.1, Cugno et al. 2019), corrected for extinction ($A_R = 0.05$; Fairlamb et al. 2015; Cugno et al. 2019).

We convert line luminosity to an estimate of the total accretion luminosity of the star using the Rigliaco et al. (2012) empirical relationship between $L_{\mathrm{H}\alpha}$ and L_{acc} derived for T-Tauri stars, namely

$$\log L_{\mathrm{acc}} = b + a \log (L_{\mathrm{H}\alpha}/L_\odot),$$

where $a = 1.25 \pm 0.07$ and $b = 2.27 \pm 0.23$. From the accretion luminosity, we derive the mass accretion rate via the standard relation:

$$\dot{M} = \left(1 - \frac{R_\star}{R_{\mathrm{in}}}\right)^{-1} \frac{L_{acc} R_\star}{G M_\star} \sim 1.25 \frac{L_{acc} R_\star}{G M_\star}$$

(Gullbring et al. 1998), assuming $R_{\mathrm{in}} \sim 5R_\star$, as in Rigliaco et al. (2012). We adopt the dynamical mass of the companion ($M_{\mathrm{B}} = 0.26 M_\odot$) and best-fit BHAC evolutionary model radius ($R_{\mathrm{B}} = 1.2 R_\odot$) from Claudi et al. (2019) to compute our final accretion rate estimate from this equation.

Table 6
HD 142572B Accretion Estimates

Date MM/DD/YY	$L_{\mathrm{H}\alpha}$ $L_\odot$	$\dot{M}$ $M_\odot\,yr^{-1}$
2013-04-11	2.12E-04	8.78E-10
2014-04-08	1.56E-04	5.99E-10
2015-05-15	1.14E-04	4.02E-10
2015-05-16	1.28E-04	4.67E-10
2015-05-18	1.36E-04	5.04E-10
2018-04-27	1.10E-04	3.84E-10

Table 6 records the line luminosities and mass accretion rates for each epoch calculated following these assumptions. The peak Hα excess, which occurs in the 2014 April 08 epoch, corresponds to a mass accretion rate estimate of $6 \times 10^{-10}\,M_\odot\,\mathrm{yr}^{-1}$.

These mass accretion rate estimates differ from those calculated by Cugno et al. (2019) ($\dot{M} = 1$–$2 \times 10^{-10}\,M_\odot\,\mathrm{yr}^{-1}$), who assumed a smaller radius ($0.9R_\odot$, given by Lacour et al. 2016). We assert that the larger radii inferred from the evolutionary model fit (Claudi et al. 2019) is more appropriate given the

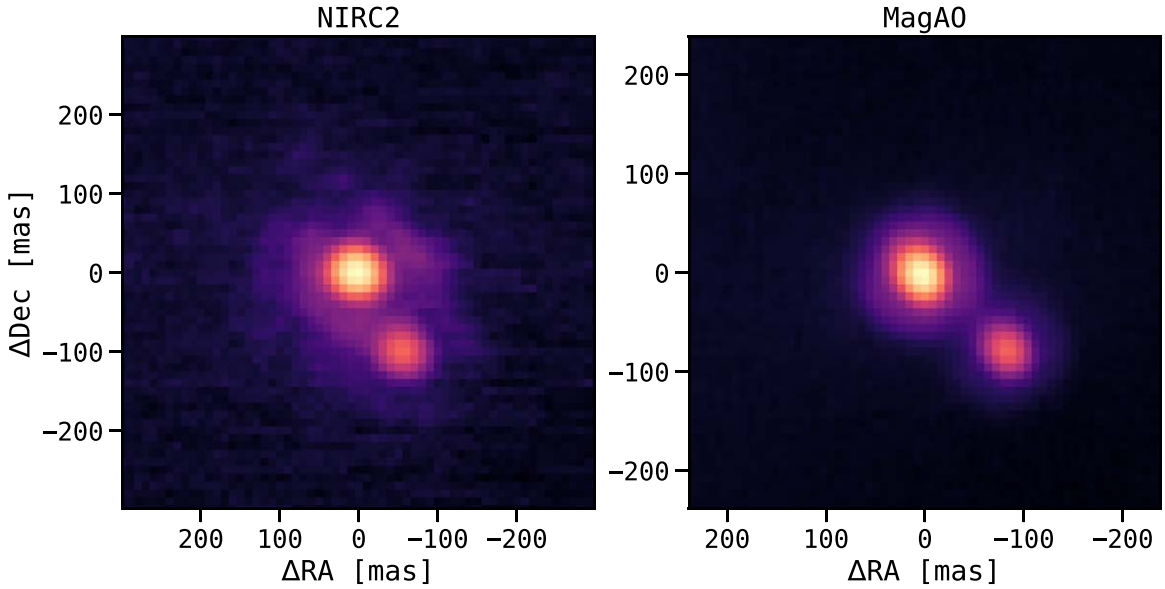

Figure 7. Representative images of θ^1 Ori B2–B3 from NIRC2 (left, NB2.108 band) and MagAO (right, z' band). All relative astrometry herein is conducted with respect to θ^1 Ori B2, which is centered at (0, 0).

purported age of the system, and this yields a slight increase in mass accretion rate estimate. The values still agree within an order of magnitude.

Our derived values are consistent with the value of $5.9 \times 10^{-10}\,M_{\odot}\,\mathrm{yr}^{-1}$ reported by Close et al. (2014a); although they adopted a lower radius of $0.29R_{\odot}$ and a mass of $0.25\,M_{\odot}$, they did not conduct the same accounting for the Hα excess of the primary, which makes up the difference. Regardless of radius assumption, all derived accretion rates lie in a range consistent with observations of accretion rates onto low-mass T-Tauri stars with masses and ages similar to those of HD 142527 B (i.e., 10^{-9}–10^{-11}; Rigliaco et al. 2012).

Variability in mass accretion rates onto the primary stars of transitional disks has been observed previously. For example, the mass accretion rate of HD 142527 A changed by a factor of seven over five yr (Mendigutía et al. 2014). Variations in mass accretion rate on the order of factors of 2–10 on timescales ranging from weeks to days have also been observed for accreting low-mass stars more generally (e.g., Robinson & Espaillat 2019). We detect only marginally significant variability in the Hα contrast of HD 142527 B given our conservative uncertainties. To our knowledge, however, this is the first detection of accretion variability in a secondary companion within a transitional disk gap.

HD 142527 B is likely surrounded by a circumsecondary disk (Lacour et al. 2016) through which accreting material is processed. This circumsecondary disk is embedded within the cavity of the larger circumbinary disk, similar to the circumplanetary disk recently observed around PDS 70 c (Benisty et al. 2021). The nondetection results from Avenhaus et al. (2017) covered in Section 2 suggest that, if circumsecondary signal exists at the position of the companion, its contribution is much smaller than our photometric errors derived from Bayesian KLIP forward modeling. This motivates the need for a high-resolution ALMA search for circumsecondary material, as was recently done in the PDS 70 system (Benisty et al. 2021).

If the observed variability of HD 142527 B was due to the rotation of an accretion hotspot in and out of view, we would expect to see detectable continuum variability, similar to that observed in the NIR, but we do not. The observed variability could also be due to an accretion column rotating in and out of view. If that was the case, we might expect to observe large-amplitude day-to-day variations between the 2015 observations, which we also do not. The simplest explanation is that the accretion rate itself is variable over time, but more data are needed to verify this and to fully understand the degree and timescale of the variability of HD 142527 B.

Observations of accretion variability in planetary-mass companions embedded within transition disk cavities have been difficult to date. The Hα lightcurve for PDS 70 b, for example, does not support large-amplitude (>30%) variability on month-long timescales (Zhou et al. 2021). Does this indicate that accretion onto objects orbiting within transition disk cavities is relatively stable when compared to accretion onto young stars? Recent modeling suggests that accretion onto a protoplanet from a circumplanetary disk may occur at a quasi-steady rate when averaged over week-long timescales, but should exhibit daily variability (Takasao et al. 2021).

The difficulty in obtaining accurate photometry of accretion emission onto planetary-mass companions limits our ability to detect variations in their Hα excess. The next generation of instruments (e.g., MagAO-X; Males et al. 2020), which can achieve higher Strehl ratios in the visible, may be able to observe such variability for a wider range of embedded companions using similar methods. Our result could indicate that accretion onto companions within cavities *is* variable at a measurable level, at least for the highest-mass companions. The caveat to this interpretation is that HD 142527 B is a stellar-mass companion whose accretion variability may be best understood in the domain of very low-mass stellar accreting objects rather than embedded planetary-mass accretors.

6. Conclusions

In this paper, we present a five-year monitoring campaign of the accreting companion HD 142527 B. We used the unique forward modeling capabilities of the Karhunen–Loeve Image

Processing (KLIP) algorithm to achieve 1–2 mas precision on astrometric measurements taken over a 6 yr time baseline, and validate an updated VisAO astrometric calibration solution (using the θ^1 Ori B2–B3 binary; see Appendix A) by demonstrating good agreement between VisAO observations of HD 142527 B and the literature. We combine literature astrometry and multi-epoch MagAO/VisAO observations to fit the orbit of HD 142527 B using `orbitize!` and derive a posterior distribution of orbital elements. We verify that the companion is on an inclined ($i = 124.^\circ85 \pm 4.^\circ56$), eccentric ($e = 0.24 \pm 0.15$) orbit and is near periastron passage. We find that the HD142527 binary has a mutual inclination with respect to the outer disk of $\theta_{\star-\mathrm{out}} = 45.87^{+2.05}_{-1.53}(^\circ)$ or $76.49^{+2.66}_{-2.72}(^\circ)$ (depending on the degenerate position of the ascending node, Ω). We also find a dramatic mutual inclination with respect to the newly directly detected inner disk, $\theta_{\mathrm{in}-\star} = 56.55^{+2.93}_{-2.79}(^\circ)$ or $66.38^{+1.84}_{-1.36}(^\circ)$. These newly derived inclinations could be used to guide hydrodynamical models of this system, in the context of disk warping, tearing, and precession in the presence of a disruptive companion.

While HD 142527 B may be too tightly separated at the time of writing to be detected without interferometric techniques, astrometry of the companion following periastron passage ($\sim$2021) will be crucial in further constraining its orbit and therefore its mass. An improved mass estimate and updated characterization could yield, among other things, more precise accretion rate estimates. A single observation with the VLTI/GRAVITY interferometer, for instance, could track the companion's periastron passage, provide an improved mass constraint, and even place estimates (or upper limits) on the Br-γ emission from HD 142527 B. With an improved mass constraint, the companion could be better compared to evolutionary models, yielding an improved age determination and a better understanding of the companion's formation. GRAVITY observations could also detect or place additional constraints on the size of the circumsecondary disk around HD 142527 B, as was done for the PDS 70 planets (Wang et al. 2021). High-resolution ALMA observations could directly detect the presence of a circumsecondary disk around B, provide constraining astrometry, and explore the inner disk surrounding A. In the future, fiber-fed spectroscopy of the companion with an instrument such as KPIC may allow for the measurement of the radial velocity, absorption, and accretion signatures of the companion at high spectral resolution, which could help constrain its currently uncertain age and spectral type (M2.5–M7).

Leveraging careful optimization of the `pyKLIP` algorithm, we achieved the most finely separated detection of a faint ($\Delta\mathrm{mag} > 6$) directly imaged companion using a non-coronagraphic, non-interferometric instrument to date. We observe clear Hα excess in all epochs of observation, corresponding to mass accretion rates similar to those observed in young, isolated M-dwarfs. We observe tentative signs of variability in the Hα excess of the companion, suggestive of accretion variability. We estimate accretion rates for the HD 142527 B companion on the order of $4\text{–}9 \times 10^{-10}\,M_\odot\,\mathrm{yr}^{-1}$, assuming a radius based on evolutionary models.

Our results demonstrate that careful, long time baseline observations from the current generation of high-contrast imaging instruments, combined with improvements in post-processing techniques, are able to place substantial constraints on both orbital motion and photometric variability, even for very tightly separated directly imaged companions, provided a self-consistent data reduction and post-processing methodology. In the future, similar observations of systems such as PDS 70, LkCa 15, and AB Aur b (and other, newly discovered accreting protoplanets) with instruments such as MagAO-X will open new windows into the time variability of protoplanetary accretion and the process by which substellar companions form and evolve.

We sincerely thank the anonymous reviewer for providing a thoughtful, rigorous, and supportive review that contributed immensely to the improvement of this paper. Special thanks to Gabriel-Dominique Marleau and Yuhiko Aoyama for their fruitful discussions of accretion physics. We thank Sarah Blunt for her tremendous help with our orbit fitting, Jason Wang for his `pyklip` expertize, as well as Connor Robinson for his encouragement. Special thanks to David Sing for his encouragement (and for letting W.O.B. use his server to run last-minute orbits). W.O.B. would like to thank Yevaud, Kalessin, and Morgoth, as well as Benjamina, Martin, Luke, Emmett, Jack, and Kate Balmer.

W.O.B. and K.B.F. acknowledge funding from NSF-AST-2009816. W.O.B. thanks the LSSTC Data Science Fellowship Program, which is funded by LSSTC, NSF Cybertraining Grant #1829740, the Brinson Foundation, and the Moore Foundation; their participation in the program has benefited this work. K.B.F.'s work on this project was also supported by a NASA Sagan fellowship. L.M.C.'s work was supported by NASA Exoplanets Research Program (XRP) grants 80NSSC18K0441 and 80NSSC21K0397. K.M.M.'s work has been supported by the NASA XRP by cooperative agreement NNX16AD44G.

This paper includes data gathered with the 6.5 meter Magellan Telescopes located at Las Campanas Observatory, Chile. Some of the data presented herein were obtained at the W.M. Keck Observatory, which is operated as a scientific partnership among the California Institute of Technology, the University of California and the National Aeronautics and Space Administration. The Observatory was made possible by the generous financial support of the W.M. Keck Foundation.

This work has made use of data from the European Space Agency (ESA) mission Gaia (https://www.cosmos.esa.int/gaia), processed by the Gaia Data Processing and Analysis Consortium (DPAC, https://www.cosmos.esa.int/web/gaia/dpac/consortium). Funding for the DPAC has been provided by national institutions, in particular the institutions participating in the Gaia Multilateral Agreement.

W.O.B. and K.B.F. would like to acknowledge that the facilities that the images used in this paper were observed from, namely Las Campanas Observatory and the Magellan Clay Telescope, are built on Diaguita land. More on the Diaguita is available from the Museo Chileno de Arte Precolombino: http://precolombino.cl/en/culturas-americanas/pueblos-originarios-de-chile/diaguita/, and additional information from Diagutia activists can be found: https://upndsalta.blogspot.com. *Astrobites* has written an informative article, "Astronomical Observatories and Indigenous Communities in Chile," which can be found here: https://astrobites.org/2019/09/10/astronomical-observatories-and-indigenous-communities-in-chile/. The W. M. Keck Observatory, and the Keck II Telescope, are built on Native Hawaiian land. We are honored to be given the opportunity to

conduct astronomy using data taken from this sacred place, and would like to point to the informative *Astrobites* articles ("Maunakea and Modern Astronomy,"https://astrobites.org/2018/11/09/maunakea-and-modern-astronomy/, "Maunakea, Western Astronomy, and Hawai'i,"https://astrobites.org/2019/08/02/maunakea-western-astronomy-and-hawaii/. We would like to encourage our colleagues to seek out additional information about the ongoing protests against additional construction on the mountain and the historical precedent for these protests.

The authors would like to acknowledge the land they have conducted research from during the course of this investigation. W.O.B. and K.B.F. would like to acknowledge the Nonotuck land Amherst College occupies, the Nonotuck ancestors, their descendants, and the neighboring Indigenous nations: the Nipmuc and the Wampanoag to the East, the Mohegan and Pequot to the South, the Mohican to the West, and the Abenaki to the North. W.O.B. would also like to acknowledge the Piscataway community, their elders and ancestors, as well as their future generations. WOB acknowledges that Johns Hopkins was founded upon the exclusions and erasures of many Indigenous peoples, including those on whose land this institution is located.

Software: `astropy` (Astropy Collaboration et al. 2013, 2018), `emcee` (Foreman-Mackey et al. 2013), `photutils` (Bradley et al. 2020), `ptemcee` (Vousden et al. 2016), `pyklip` (Wang et al. 2015), `orbitize!` (Blunt et al. 2020).

Appendix A
Astrometric Calibration of VisAO

Given the precision ($\lesssim$1 mas) afforded by BKA and other methods, the dominant source of error on the astrometry of directly imaged companions is often the absolute astrometric calibration of the instrument. In order to ensure our astrometric measurements of HD 142527 B were accurate when compared to literature astrometry, it was necessary to conduct an epoch-to-epoch calibration to determine the stability of the absolute astrometry of VisAO over time.

The astrometric calibration of an instrument such as VisAO is nontrivial due to the instrument's small FOV ($8'' \times 8''$) and because MagAO is a natural guide star adaptive optics system, which requires a bright target ($R_{\rm mag} < 15$) within the field to make effective wave front corrections. This significantly limits the number of viable calibration fields available to the observer.

Previous astrometric solutions for VisAO (Close et al. 2013; Males et al. 2014) have been calculated by cross-referencing MagAO/VisAO images with LBT/PISCES images of the dense Trapezium cluster (Close et al. 2012). The astrometric solution of PISCES was itself derived from cross-referencing against HST/ACS images of the cluster (Ricci et al. 2008). There is non-negligible orbital motion in these systems (Close et al. 2013) that needs to be accounted for in images taken months to years apart.

Additionally, VisAO is removed and remounted between observing runs, which introduces epoch-to-epoch uncertainty in its calibration. Until now, VisAO users have operated under the assumption that the astrometric calibration has remained stable between mountings since 2013, adopting the most recent published calibration of the instrument from Males et al. (2014), who find a platescale of 7.8596 ± 0.0019 mas pix^{-1} and an offset from north of $0\overset{\circ}{.}59 \pm \sim 0\overset{\circ}{.}3$ clockwise based on Trapezium data collected in the Ys filter.

We measured the VisAO astrometric solution by cross-comparing VisAO astrometry with an orbit fit to Keck/NIRC2 images[18] of the θ^1 Ori B2–B3 binary obtained between 2001 and Jan. 2020. The data were corrected for nonlinearity, dark-subtracted, flatfielded, and bad-pixel-corrected before being corrected for geometric distortion, as described in De Rosa et al. (2020). The NIRC2 astrometric solution is tied to precise HST/ACS observations of SiO masers in the Galactic Center (Yelda et al. 2010; Service et al. 2016).

Our calibration method follows De Rosa et al. (2020), who conducted a similar calibration of the Gemini Planet Imager (GPI) using the same Keck/NIRC2 images. We measure the position of the θ^1 Ori B2–B3 binary across more than 20 yr of NIRC2 imagery using `photutils` PSF photometry (Bradley et al. 2020). We used the PSF of θ^1 Ori B1 to conduct PSF photometry, fitting both components of the binary jointly with `orbitize!`, which allows us to determine the expected position of the binary at arbitrary epochs and accounts for nonlinear orbital motion over time. Our observations of HD 142527 and our VisAO calibration images of the θ^1 Ori B system fall within the NIRC2 baseline of observations, meaning that each comparison is made within a well-constrained orbital fit. Figure 7 shows two representative images of θ^1 Ori B2–B3 from NIRC2 and MagAO, respectively.

We initialized an `oribitze!` MCMC with 50 walkers, which each took 100,000 steps after 100,000 "burn-in" steps were discarded, for a total of five million accepted fit orbits. We set the initial total system mass to be $5.5 \pm 0.5 M_{\odot}$ (Close et al. 2013) and the initial system parallax to 2.655 ± 0.042 (Gaia Collaboration et al. 2021). We then determined the platescale and North Angle offset in each data set by comparing the separation and Position Angle of the B2–B3 binary in VisAO images of the system to the expected separation and Position Angle of the NIRC2 orbital fit. The VisAO images of the θ^1 Ori B system were reduced and registered following the methods described in Section 3, and the positions were measured using `photutils` PSF photometry.

We determined the platescale and North Angle offset for each data set, then took the average of each data set weighted by the measurement uncertainty. We observe no significant variations in platescale or North Angle offset over time or between filters, and conclude that both have remained stable across instrument mountings. Our measurements of each therefore represent observations of a constant over time, and we take the weighted average of measurements from individual epochs to be the most precise estimate of the true platescale and North Angle for VisAO.

We find the updated VisAO platescale to be 7.95 ± 0.010 mas pix^{-1} and the North Angle offset to be $0\overset{\circ}{.}497 \pm 0\overset{\circ}{.}192$ counterclockwise. Our updated calibration yields updated errors, and we find (similarly to De Rosa et al.) slightly larger errors on the platescale than previous calibrations, and smaller errors on the North Angle offset. It would appear that, by measuring the platescale in only one filter with a limited number of observations, previous calibrations underestimated the platescale error, and that a longer baseline of observations allows improved precision in determination of the North Angle offset.

Figure 8 plots measurements of the VisAO platescale over time and across multiple filters. Figure 9 shows the orbital fit to

[18] These data are available from the Keck Observatory Archive (KOA) at koa.ipac.caltech.edu.

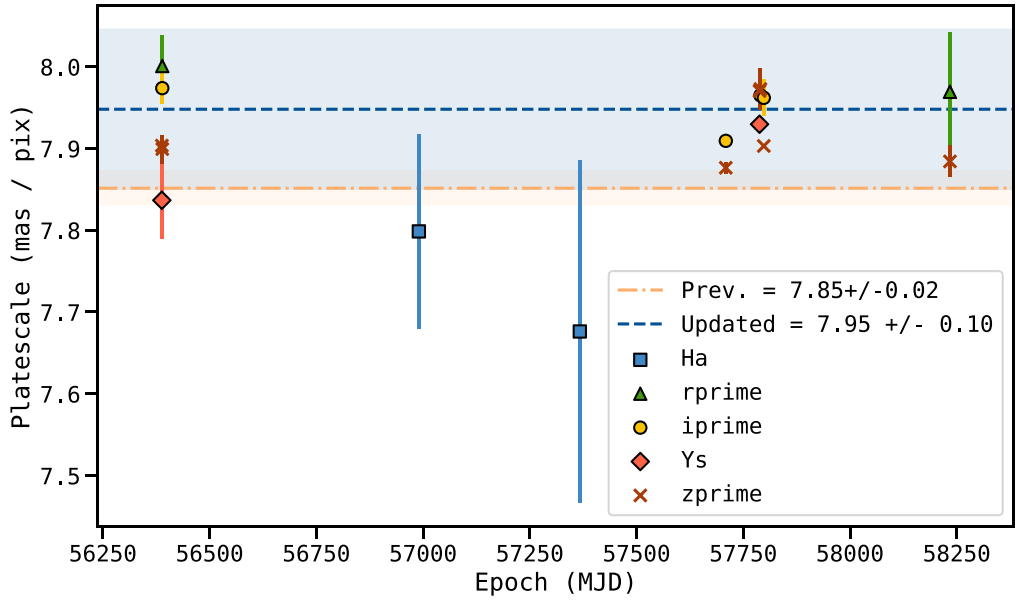

Figure 8. VisAO platescale as measured in various VisAO filters over time. The orange shaded region, centered on the horizontal orange dashed–dotted line, represents the previous astrometric solution of Males et al. (2014) using data taken in the Ys filter in 2014. Note the agreement between our measurement of the same Ys data (red diamond) and their value. We note that the Hα observations suffered from poor observing conditions and an unfavorable observing strategy for astrometry, which resulted in very low signal-to-noise on the B2–B3 pair. No obvious trend in platescale with wavelength or time is present, and therefore we adopt the weighted average and standard deviation on the weighted average (represented by the blue dashed line and shaded region, respectively) as the updated platescale and platescale error for the instrument.

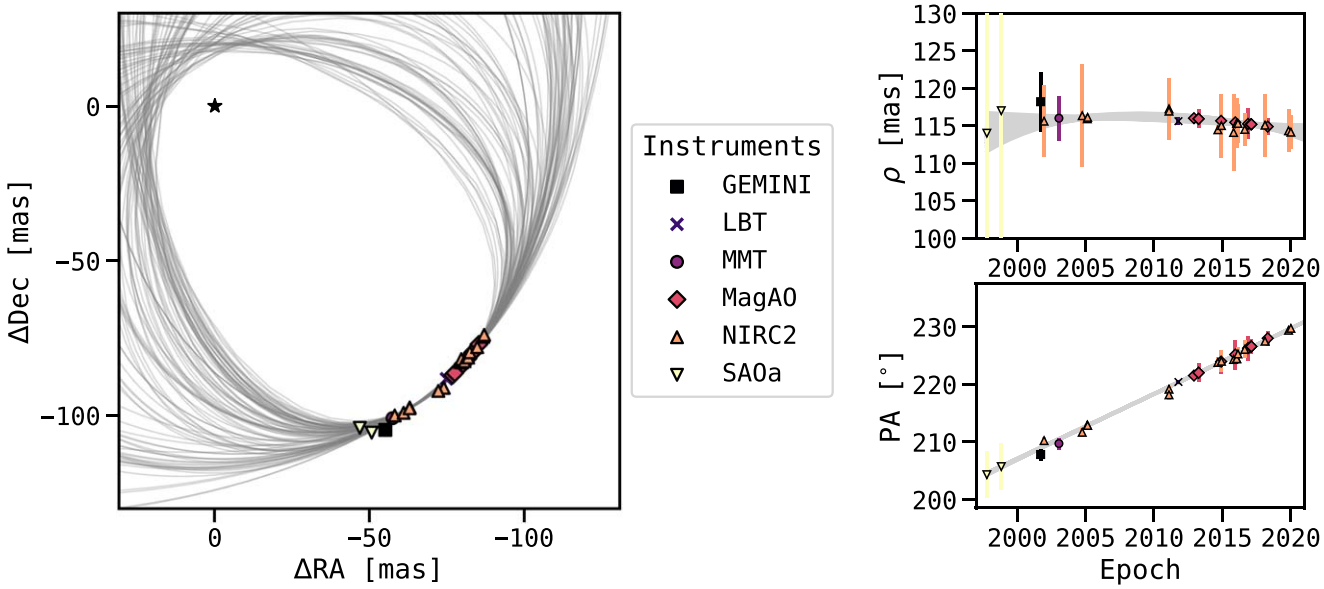

Figure 9. Five hundred orbital fits to the NIRC2 astrometry of θ^1 Ori B2–B3 randomly drawn from the posterior distribution. Astrometry compiled in Table 7 is overplotted. Only the NIRC2 astrometry (orange triangles) was used to fit the orbit of the binary, and the corrected VisAO astrometry (red diamonds) falls along the fit orbits by design.

the NIRC2 observations of θ^1 Ori B2–B3 and updated VisAO astrometry of the binary pair.

As a byproduct of this astrometric calibration, we have obtained astrometric measurements of the θ^1 Ori B2–B3 over nearly 20 yr, as well as an updated, well-defined orbital solution for the binary. We record the astrometry from both NIRC2 and VisAO with other literature astrometry in Table 7. We record the orbital elements as drawn from the posterior distribution of fits to the NIRC2 astrometry in Table 8.

Table 7
θ^1 Ori B2–B3 Astrometry

Epoch (MJD)	Separation (mas)	Position Angle (°)	Instrument	PI
50735	114.000 ± 0.050	204.300 ± 4.000	SAOa	Weigelt et al. (1999)
51120	117.000 ± 0.005	205.700 ± 4.000	SAOa	Weigelt et al. (1999)
52171	118.200 ± 0.004	207.800 ± 1.000	GEMINI	Close et al. (2003)
52263	115.600 ± 4.766	210.212 ± 0.595	NIRC2	This work
52659	116.000 ± 0.003	209.700 ± 1.000	MMT	Close et al. (2003)
53281	116.329 ± 6.831	211.649 ± 0.768	NIRC2	This work
53417	115.919 ± 0.444	212.922 ± 0.165	NIRC2	This work
53426	116.109 ± 0.112	212.840 ± 0.030	NIRC2	This work
55850	115.600 ± 0.001	220.390 ± 0.300	LBT	Close et al. (2012)
55598	117.249 ± 4.133	219.128 ± 0.543	NIRC2	This work
55598	116.936 ± 1.880	218.154 ± 0.943	NIRC2	This work
56265	116.000 ± 0.000	221.500 ± 0.300	MagAO	Close et al. (2013)
56388	115.914 ± 1.223	221.989 ± 1.584	MagAO	This work
56389	115.914 ± 1.015	221.992 ± 1.047	MagAO	This work
56990	115.648 ± 0.550	223.931 ± 2.079	MagAO	This work
56903	114.453 ± 0.557	223.776 ± 0.860	NIRC2	This work
56997	115.012 ± 4.235	223.980 ± 1.871	NIRC2	This work
57322	114.090 ± 5.086	224.290 ± 0.694	NIRC2	This work
57367	115.447 ± 1.301	225.152 ± 2.603	MagAO	This work
57405	115.318 ± 3.311	224.424 ± 0.662	NIRC2	This work
57405	115.318 ± 3.311	224.424 ± 0.662	NIRC2	This work
57439	115.296 ± 2.548	225.253 ± 1.120	NIRC2	This work
57620	114.498 ± 2.178	226.040 ± 1.549	NIRC2	This work
57709	115.239 ± 2.008	226.264 ± 2.108	MagAO	This work
57788	115.188 ± 0.116	226.521 ± 0.498	MagAO	This work
57790	115.187 ± 0.117	226.527 ± 0.526	MagAO	This work
57798	115.182 ± 0.673	226.554 ± 1.218	MagAO	This work
58162	115.067 ± 4.193	227.458 ± 0.558	NIRC2	This work
58234	114.875 ± 1.121	227.979 ± 1.218	MagAO	This work
58790	114.316 ± 2.814	229.360 ± 0.561	NIRC2	This work
58852	114.130 ± 2.234	229.690 ± 0.003	NIRC2	This work

Notes. SAOa speckle interferometry from Weigelt et al. (1999), and GEMINI, MMT, and LBT direct imaging from Close et al. (2003, 2012, 2013). Note that the MagAO measurements presented here are not independent measurements, as they were tied to the orbit fit to NIRC2 observations in order to determine the platescale and North Angle offset.

Table 8
θ^1 Ori B2–B3 Orbital Elements

Element	Value
a (au)	$42.23^{+2.83}_{-1.38}$
e	$0.72^{+0.02}_{0.02}$
i (°)	$53.64^{+0.98}_{-0.90}$
ω(°)	91.09 ± 2.26, 271.05 ± 2.31
Ω(°)	114.18 ± 13.00, 293.07 ± 13.36
Periastron (yr)	$2059.17^{+5.11}_{-4.07}$
Parallax (mas)	$2.65^{+0.04}_{-0.04}$
$M_{\rm total}(M_\odot)$	$5.44^{+0.48}_{-0.46}$

Appendix B
Forward Model Choice and VisAO Ghost Calibration

The VisAO CCD saturates at ∼16,000 counts, and because of its small FOV, there are no other stars within the field that can be used as a PSF to forward model. There are no artificial satellite spots injected as astrometric or photometric calibrators, but there is an instrumental "ghost" PSF that appears to the right of the natural guide star in each image (see Figure 10). We investigated the stability of the ghost and the scaling relationships between the ghost and central PSF using 10 unsaturated data sets taken as part of the GAPlanetS survey (Follette et al. 2017; K. B. Follette et al. 2022, in preparation).

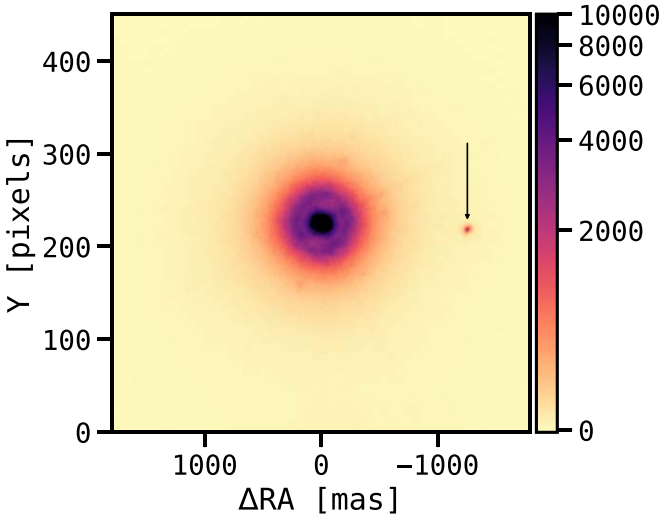

Figure 10. A saturated image of HD 142527. The position of the instrumental ghost is marked with a black arrow. The *Y*-axis is in pixels, and the *X*-axis is labeled in milliarcseconds to illustrate the spatial extent of the 451 pixel crop and the position of the ghost.

We find that peak of the ghost varies consistently with the peak of the central PSF. We adopt the empirical scaling relationships $F_{c,\mathrm{H}\alpha} = 179.68 \pm 4.59 \times F_{g,\mathrm{H}\alpha}$ and $F_{c,\mathrm{cont.}} = 196.31 \pm 3.56 \times F_{g,\mathrm{cont.}}$ However, we find that, when fit with a Moffat distribution, the FWHM of the ghost is on average 7% larger than that of the central PSF. We therefore adopt the relationship $\mathrm{FWHM}_c = 0.93 \times \mathrm{FWHM}_{\mathrm{ghost}}$ in determining the FWHM of saturated images.

This ghost calibration was conducted in part because we had initially used the instrumental ghost as a forward model PSF, and found it to be a poor fit. We then investigated the best choice of forward model for saturated data by comparing sum-of-squares residuals for the ghost itself, a Moffat distribution fit to the ghost, a Gaussian distribution fit to the ghost, and both distributions (Moffat and Gaussian) with reduced FWHM equal to $0.93 \times \mathrm{FWHM}_{\mathrm{ghost}}$. For each PSF, we conducted the same procedure as in Section 4, forward modeling the PSF through KLIP and fitting it to the known companion, resulting in a posterior distribution of fits and a residual map. We found that, for the majority of our images of HD 142527 B, Gaussian PSFs yielded the smallest residuals. We assume that, scaling by the above relationships, the counts under the Gaussian are equivalent to those under the unsaturated central PSF. This then enables us to conduct photometry using BKA.

Appendix C
Forward Model Fits

Optimized post-KLIP images for each detection epoch, best-fit BKA models, and the residuals between them are shown for HD 142527 B in the Hα and continuum filters in Figures 11 and 12, respectively. The marginal posterior distributions for the BKA fits, examples of which are shown in Figure 13, are

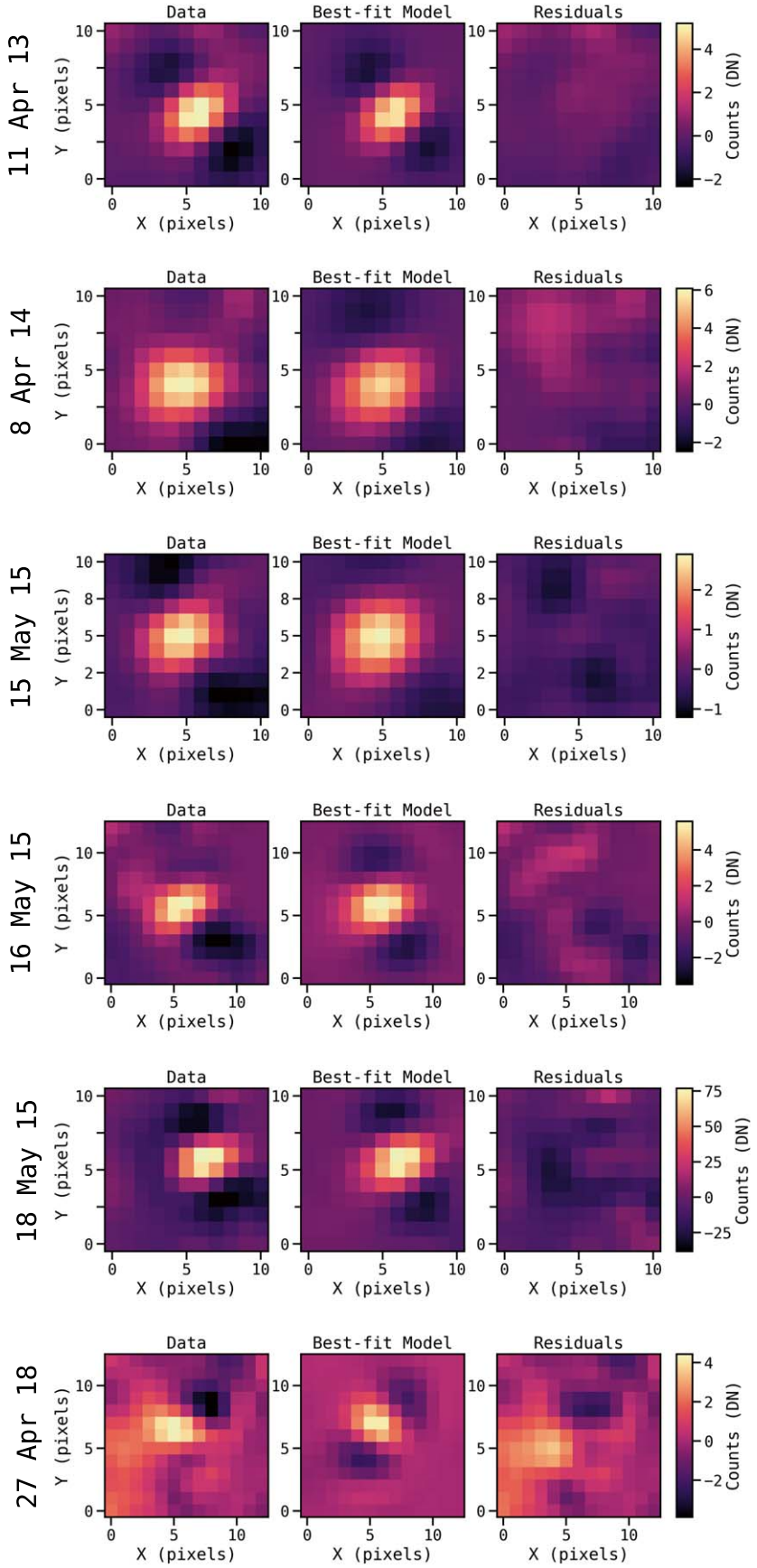

Figure 11. A gallery of BKA forward model best fits to HD 142527 B in the Hα filter, in chronological order from top to bottom. Data (left) are fit by BKA, yielding a best-fit forward model (center) and their difference (right).

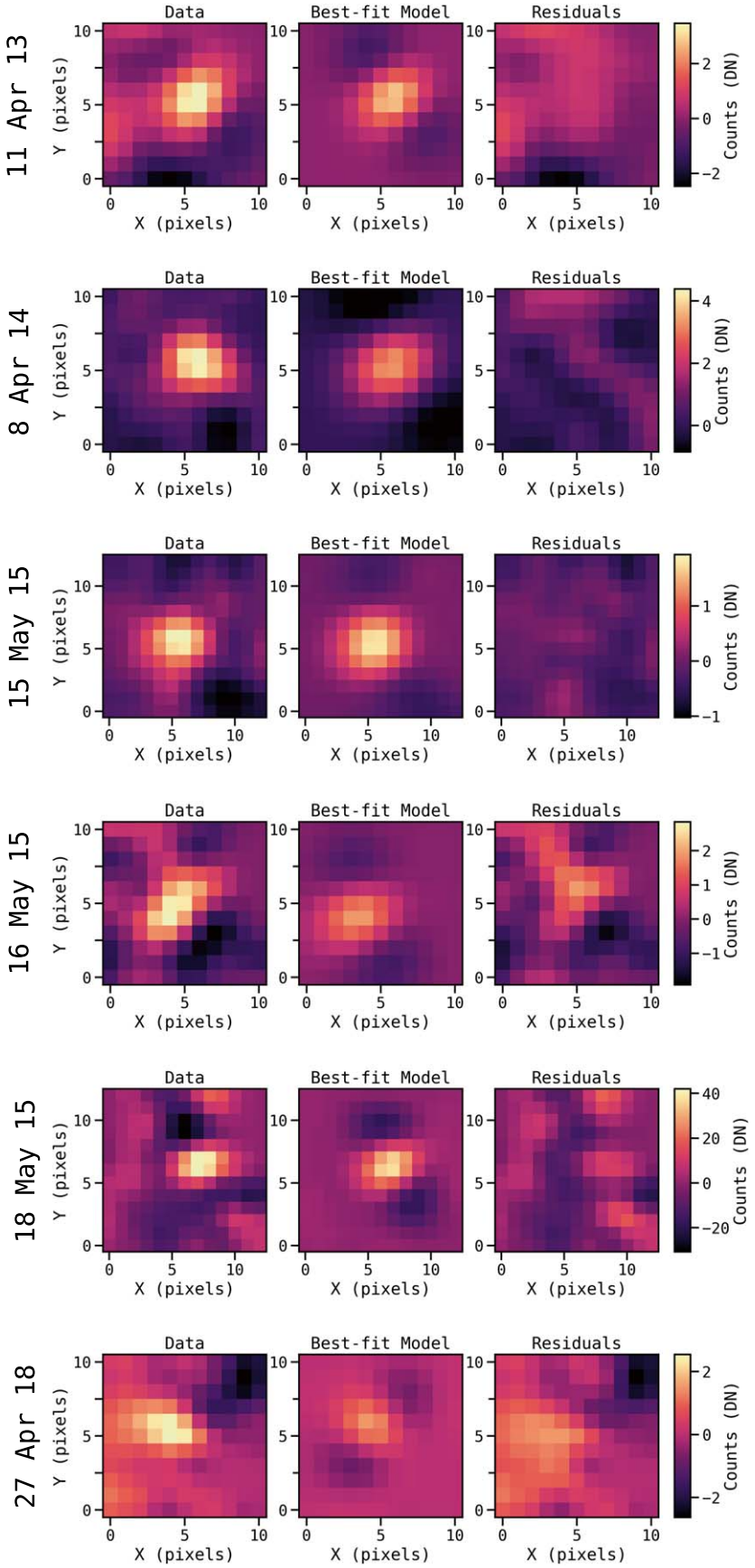

Figure 12. A gallery of BKA forward model best fits to HD 142527 B in the continuum filter, in chronological order from top to bottom. Data (left) are fit by BKA, yielding a best-fit forward model (center) and their difference (right).

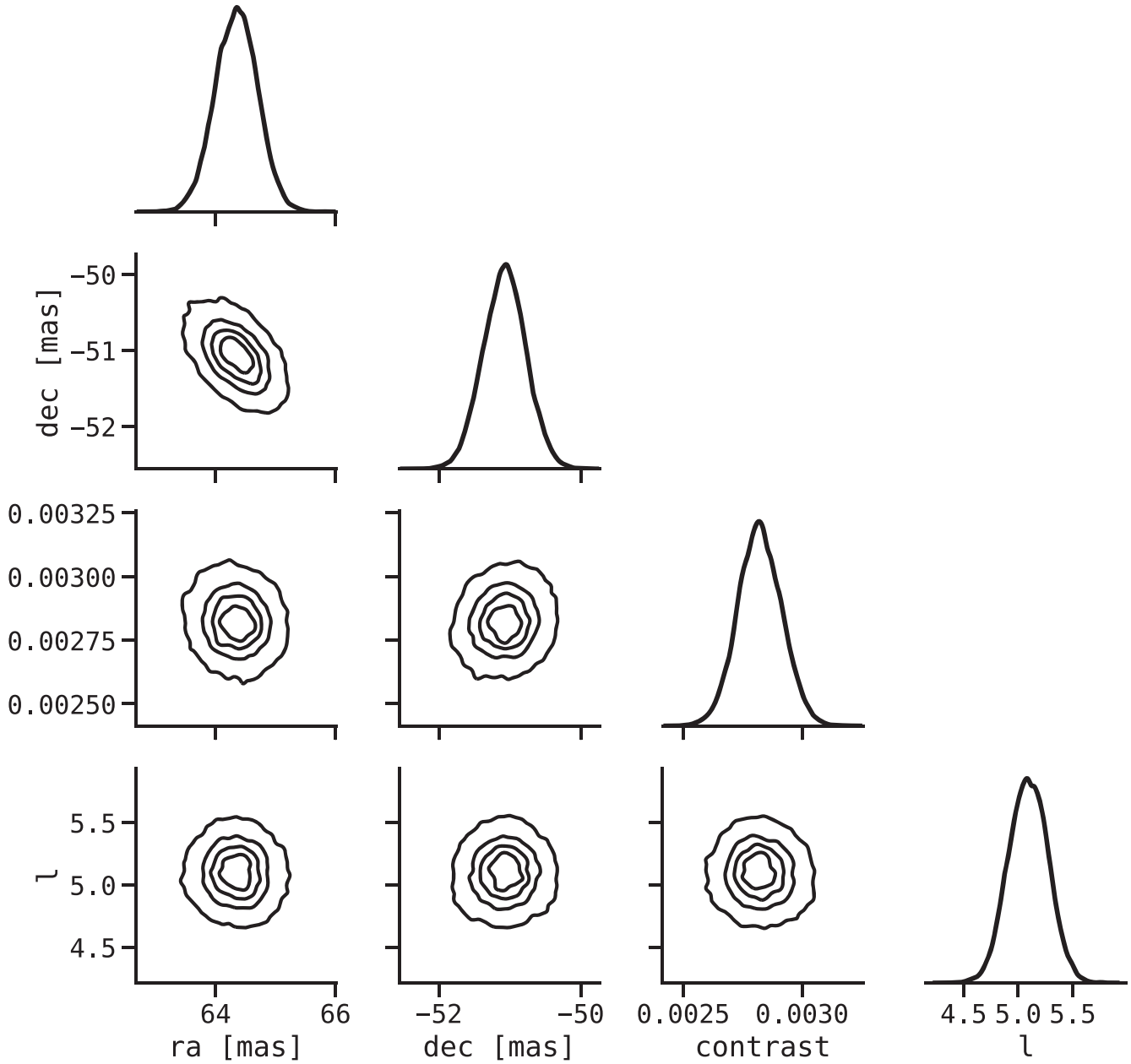

Figure 13. A corner plot illustrating the posterior distribution of BKA forward model fits to the 2013 April 11 Hα data, which are representative of all other epochs. Note that all marginal parameters are normally distributed, and the only correlation is a slight linear correlation between the X and Y positions.

distributed normally for all epochs. The most common correlation is a slight linear correlation between the X and Y positions (as seen in Figure 13).

Appendix D
Orbit Fit Posteriors

This appendix details posterior distributions of orbital elements for our astrometric fits, computed using `orbitize!`. Figure 14 illustrates the posterior distribution of orbital elements for the HD 142527 AB binary. Figure 15 plots the mutual inclination parameters $i_\star$, $\Omega_\star$ from Figure 14, computed as described in Section 5, along with i_d, Ω_d drawn from Gaussian distributions specified by the disk parameters fit by Bohn et al. (2022), and the resultant distribution of mutual inclinations θ. Figure 16 illustrates the posterior distribution for the orbit of the θ^1 Ori B2–B3 derived from Keck NIRC2 observations, as described in Appendix A.

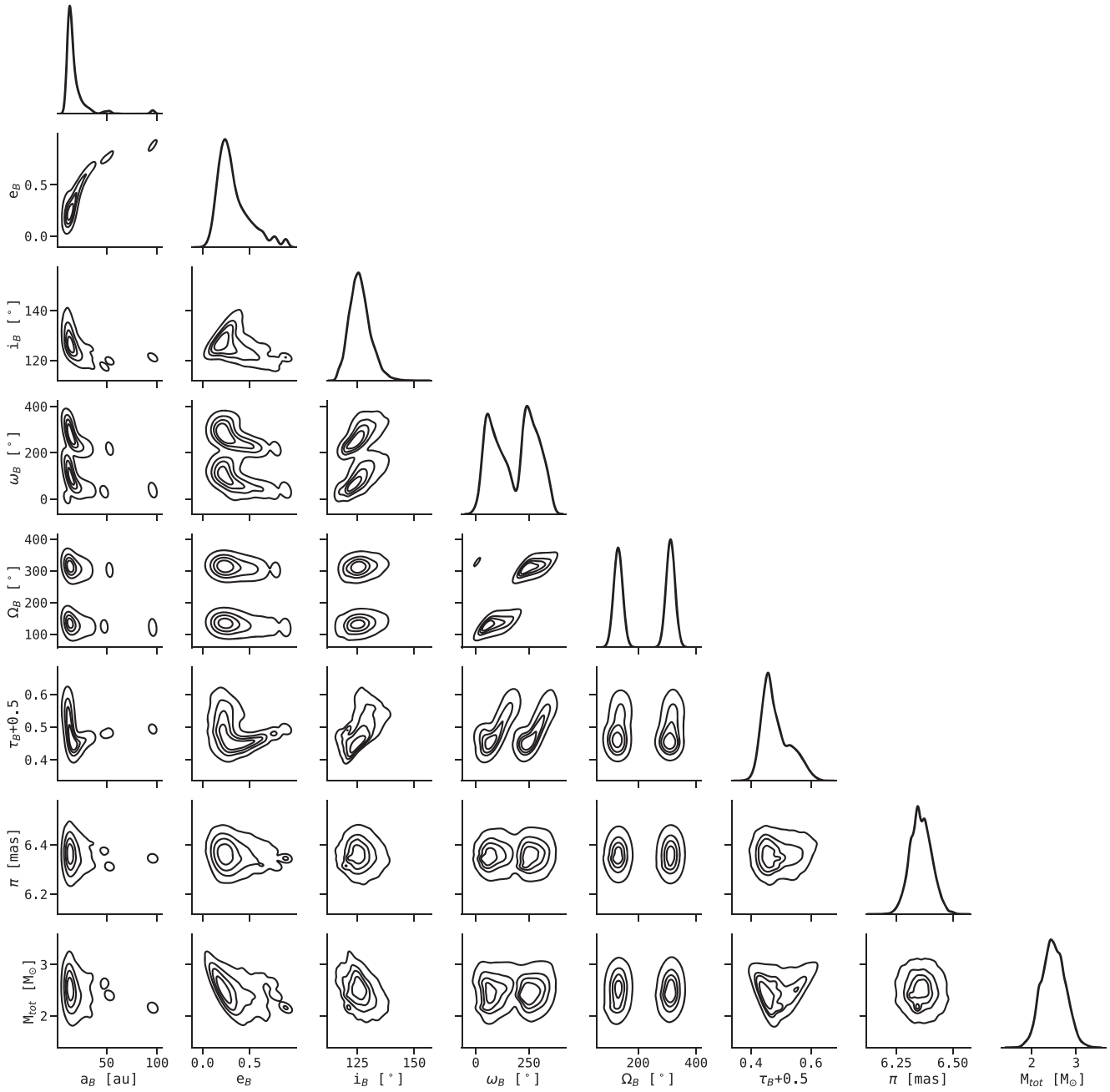

Figure 14. Posterior distribution of orbital elements fit to the astrometry of HD 142527 B. Here, ω and Ω show bimodal distributions with peaks spaced 180° apart; this a known degeneracy in visual orbits with a lack of RV constraints.

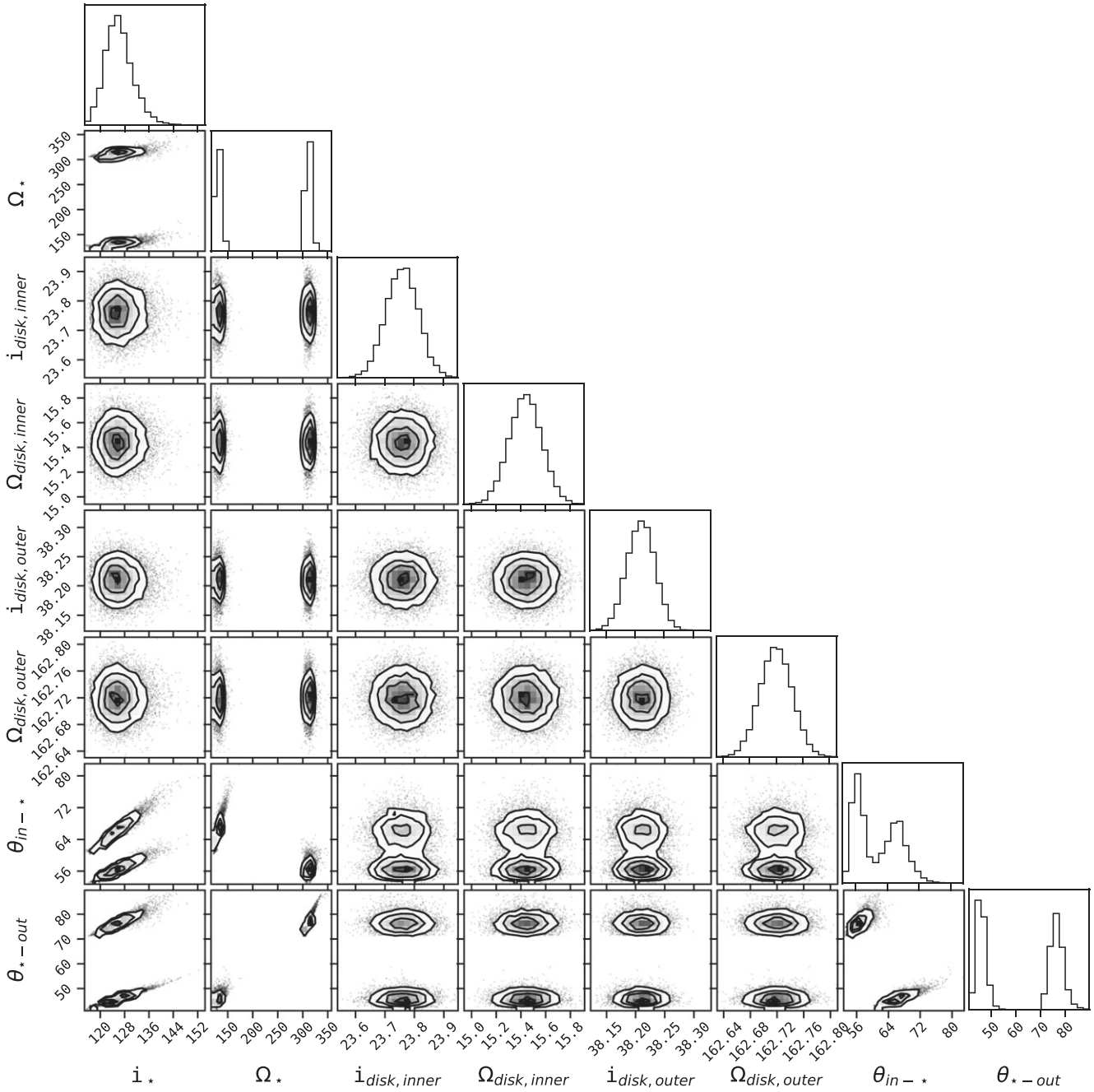

Figure 15. Posterior distribution of fit ($i_\star$, $\Omega_\star$) and randomly sampled ($i_{\rm disk}$, $\Omega_{\rm disk}$) for both inner and outer disks yields a posterior distribution of θ, the mutual inclination angle between the binary orbit and the disk component. As in Czekala et al. (2019), the mutual inclination of the outer disk for this system is multimodal, but dramatically misaligned ($\theta \gg 3^\circ$) regardless of the choice of $\Omega_\star$. Interestingly, one family of $\theta_{\star-{\rm out}}$ is nearly perpendicular, similar to the configuration described in Price et al. (2018).

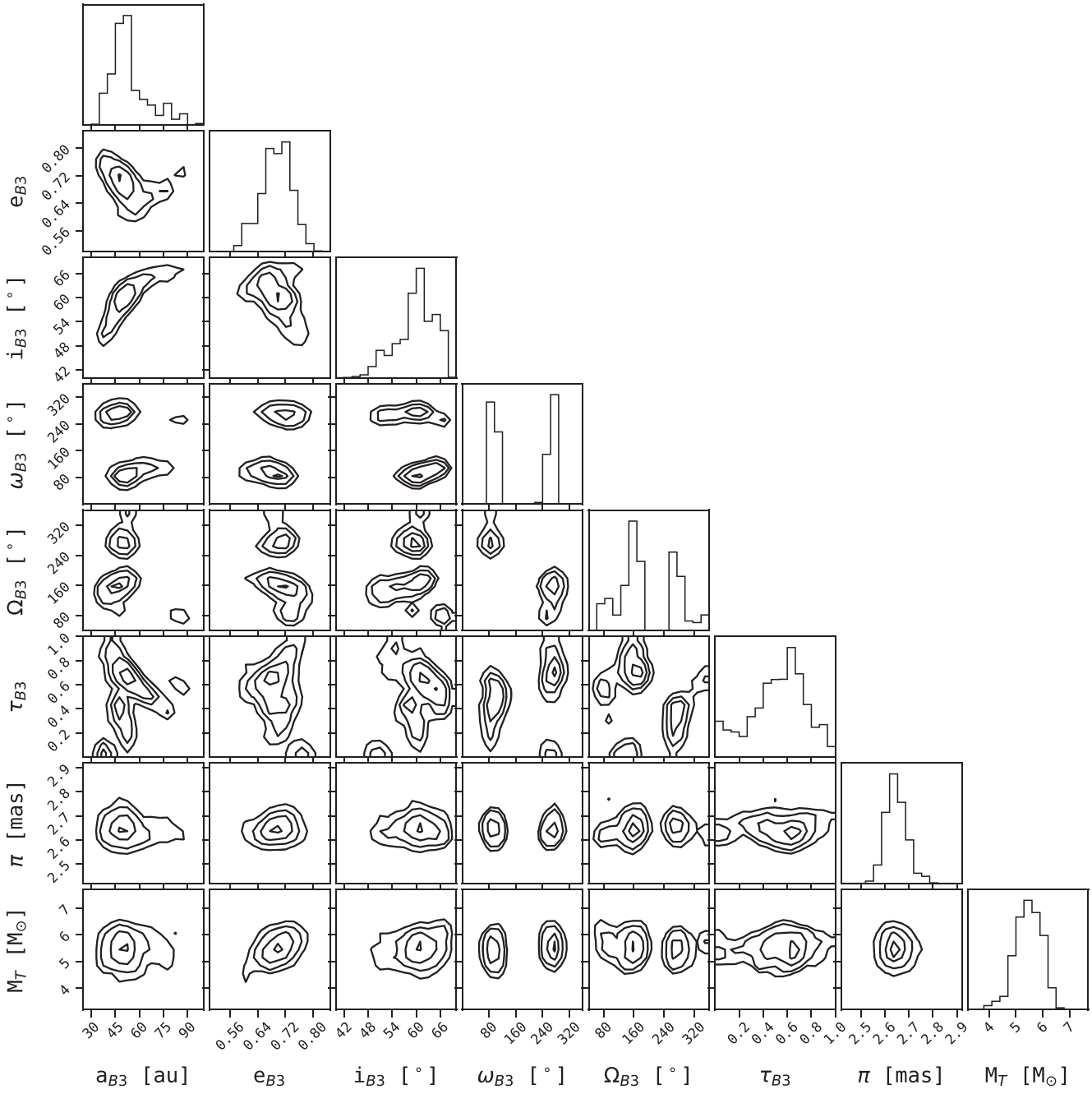

Figure 16. Posterior distribution of orbital elements fit to NIRC2 astrometry of θ^1 Ori B2–B3. The fit displays a posterior distribution typical of short-arc visual orbit fits, with the same bimodal ω and Ω noted previously, normally distributed π and $M_{\rm tot}$, correlated semimajor axis, eccentricity, and inclinations that are otherwise relatively constrained. This orbit is so satisfyingly typical that I have petitioned for it act as the unofficial mascot of `orbitize!`, but I have not yet been humored thusly.

ORCID iDs

William O. Balmer https://orcid.org/0000-0001-6396-8439
Katherine B. Follette https://orcid.org/0000-0002-7821-0695
Laird M. Close https://orcid.org/0000-0002-2167-8246
Jared R. Males https://orcid.org/0000-0002-2346-3441
Robert J. De Rosa https://orcid.org/0000-0002-4918-0247
Jéa I. Adams Redai https://orcid.org/0000-0002-4489-3168
Alycia J. Weinberger https://orcid.org/0000-0001-6654-7859
Katie M. Morzinski https://orcid.org/0000-0002-1384-0063
Julio Morales https://orcid.org/0000-0001-7525-7423
Kimberly Ward-Duong https://orcid.org/0000-0002-4479-8291
Laurent Pueyo https://orcid.org/0000-0003-3818-408X

References

Aly, H., Gonzalez, J.-F., Nealon, R., et al. 2021, MNRAS, 508, 2743
Aoyama, Y., Marleau, G.-D., Ikoma, M., & Mordasini, C. 2021, ApJL, 917, L30
Astropy Collaboration, Price-Whelan, A. M., Sipőcz, B. M., et al. 2018, AJ, 156, 123
Astropy Collaboration, Robitaille, T. P., Tollerud, E. J., et al. 2013, A&A, 558, A33
Avenhaus, H., Quanz, S. P., Garufi, A., et al. 2018, ApJ, 863, 44

Avenhaus, H., Quanz, S. P., Schmid, H. M., et al. 2014, ApJ, 781, 87
Avenhaus, H., Quanz, S. P., Schmid, H. M., et al. 2017, AJ, 154, 33
Bae, J., Pinilla, P., & Birnstiel, T. 2018, ApJL, 864, L26
Benisty, M., Bae, J., Facchini, S., et al. 2021, ApJL, 916, L2
Biller, B., Lacour, S., Juhász, A., et al. 2012, ApJL, 753, L38
Blunt, S., Wang, J. J., Angelo, I., et al. 2020, AJ, 159, 89
Boehler, Y., Ménard, F., Robert, C. M. T., et al. 2021, A&A, 650, A59
Boehler, Y., Weaver, E., Isella, A., et al. 2017, ApJ, 840, 60
Bohn, A. J., Benisty, M., Perraut, K., et al. 2022, A&A, 658, A183
Bowler, B. P., Blunt, S. C., & Nielsen, E. L. 2020, AJ, 159, 63
Bradley, L., Sipőcz, B., Robitaille, T., et al. 2020, astropy/photutils: 1.0.0, 1.0.0, Zenodo, doi: 10.5281/zenodo.4044744
Buchner, J., Georgakakis, A., Nandra, K., et al. 2014, A&A, 564, A125
Casassus, S., Marino, S., Pérez, S., et al. 2015, ApJ, 811, 92
Casassus, S., van der Plas, G. M., Perez, S., et al. 2013, Natur, 493, 191
Christiaens, V., Casassus, S., Absil, O., et al. 2018, A&A, 617, A37
Claudi, R., Maire, A. L., Mesa, D., et al. 2019, A&A, 622, A96
Close, L. M. 2020, AJ, 160, 221
Close, L. M., Follette, K. B., Males, J. R., et al. 2014a, ApJL, 781, L30
Close, L. M., Males, J. R., Follette, K. B., et al. 2014b, Proc. SPIE, 9148, 91481M
Close, L. M., Males, J. R., Morzinski, K., et al. 2013, ApJ, 774, 94
Close, L. M., Puglisi, A., Males, J. R., et al. 2012, ApJ, 749, 180
Close, L. M., Wildi, F., Lloyd-Hart, M., et al. 2003, ApJ, 599, 537
Cugno, G., Quanz, S. P., Hunziker, S., et al. 2019, A&A, 622, A156
Currie, T., Lawson, K., Schneider, G., et al. 2022, NatAs, Advanced Online Publication
Currie, T., Marois, C., Cieza, L., et al. 2019, ApJL, 877, L3
Czekala, I., Chiang, E., Andrews, S. M., et al. 2019, ApJ, 883, 22
De Rosa, R. J., Nguyen, M. M., Chilcote, J., et al. 2020, JATIS, 6, 015006
Dodson-Robinson, S. E., & Salyk, C. 2011, ApJ, 738, 131
Dong, R., & Fung, J. 2017, ApJ, 835, 146
Eisenhauer, F., Abuter, R., Bickert, K., et al. 2003, Proc. SPIE, 4841, 1548
Espaillat, C., Muzerolle, J., Najita, J., et al. 2014, in Protostars and Planets VI, ed. H. Beuther et al., 497 (Tuscon, AZ: Univ. of Arizona Press)
Esposito, T. M., Kalas, P., Fitzgerald, M. P., et al. 2020, AJ, 160, 24
Facchini, S., Juhász, A., & Lodato, G. 2018, MNRAS, 473, 4459
Fairlamb, J. R., Oudmaijer, R. D., Mendigutía, I., Ilee, J. D., & van den Ancker, M. E. 2015, MNRAS, 453, 976
Feroz, F., Hobson, M. P., & Bridges, M. 2009, MNRAS, 398, 1601
Follette, K. B., Rameau, J., Dong, R., et al. 2017, AJ, 153, 264
Foreman-Mackey, D., Hogg, D. W., Lang, D., & Goodman, J. 2013, PASP, 125, 306
Fukagawa, M., Tamura, M., Itoh, Y., et al. 2006, ApJL, 636, L153
Gaia Collaboration, Brown, A. G. A., Vallenari, A., et al. 2021, A&A, 649, A1
Garg, H., Pinte, C., Christiaens, V., et al. 2021, MNRAS, 504, 782
Garufi, A., Avenhaus, H., Pérez, S., et al. 2020, A&A, 633, A82
Golomb, J., Rocha, G., Meshkat, T., et al. 2019, arXiv:1912.01232
Greenbaum, A. Z., Cheetham, A., Sivaramakrishnan, A., et al. 2019, AJ, 157, 249
Gullbring, E., Hartmann, L., Briceño, C., & Calvet, N. 1998, ApJ, 492, 323
Haffert, S. Y., Bohn, A. J., de Boer, J., et al. 2019, NatAs, 3, 749
Hashimoto, J., Aoyama, Y., Konishi, M., et al. 2020, AJ, 159, 222
Hunziker, S., Schmid, H. M., Ma, J., et al. 2021, A&A, 648, A110
Keppler, M., Benisty, M., Müller, A., et al. 2018, A&A, 617, A44
Kostov, V. B., Orosz, J. A., Feinstein, A. D., et al. 2020, AJ, 159, 253
Kostov, V. B., Powell, B. P., Orosz, J. A., et al. 2021, AJ, 162, 234
Kraus, A. L., Ireland, M. J., Huber, D., Mann, A. W., & Dupuy, T. J. 2016, AJ, 152, 8
Lacour, S., Biller, B., Cheetham, A., et al. 2016, A&A, 590, A90
Lenzen, R., Hartung, M., Brandner, W., et al. 2003, Proc. SPIE, 4841, 944
Macintosh, B., Graham, J. R., Ingraham, P., et al. 2014, PNAS, 111, 12661
Males, J. R., Close, L. M., Guyon, O., et al. 2020, Proc SPIE, 11448, 114484L
Males, J. R., Close, L. M., Morzinski, K. M., et al. 2014, ApJ, 786, 32
Marino, S., Perez, S., & Casassus, S. 2015, ApJL, 798, L44
Marleau, G.-D., Aoyama, Y., Kuiper, R., et al. 2022, A&A, 657, A38
Mendigutía, I., Fairlamb, J., Montesinos, B., et al. 2014, ApJ, 790, 21
Mordasini, C., Marleau, G. D., & Mollière, P. 2017, A&A, 608, A72
Morzinski, K. M., Close, L. M., Males, J. R., et al. 2016, Proc. SPIE, 9909, 990901
Ohashi, N. 2008, Ap&SS, 313, 101
Perez, S., Casassus, S., Ménard, F., et al. 2015, ApJ, 798, 85
Price, D. J., Cuello, N., Pinte, C., et al. 2018, MNRAS, 477, 1270
Pueyo, L. 2016, ApJ, 824, 117
Ricci, L., Robberto, M., & Soderblom, D. R. 2008, AJ, 136, 2136
Rigliaco, E., Natta, A., Testi, L., et al. 2012, A&A, 548, A56
Robinson, C. E., & Espaillat, C. C. 2019, ApJ, 874, 129
Rodigas, T. J., Follette, K. B., Weinberger, A., Close, L., & Hines, D. C. 2014, ApJL, 791, L37
Rousset, G., Lacombe, F., Puget, P., et al. 2003, Proc. SPIE, 4839, 140
Sallum, S., Follette, K. B., Eisner, J. A., et al. 2015, Natur, 527, 342
Service, M., Lu, J. R., Campbell, R., et al. 2016, PASP, 128, 095004
Stauffer, J., Cody, A. M., Baglin, A., et al. 2014, AJ, 147, 83
Stolker, T., Haffert, S. Y., Kesseli, A. Y., et al. 2021, AJ, 162, 286
Szulágyi, J., & Ercolano, B. 2020, ApJ, 902, 126
Takasao, S., Aoyama, Y., & Ikoma, M. 2021, ApJ, 921, 10
Tamura, M. 2016, PJAB, 92, 45
Verhoeff, A. P., Min, M., Pantin, E., et al. 2011, A&A, 528, A91
Vousden, W. D., Farr, W. M., & Mandel, I. 2016, MNRAS, 455, 1919
Wagner, K., Follete, K. B., Close, L. M., et al. 2018, ApJL, 863, L8
Wang, J. J., Graham, J. R., Pueyo, L., et al. 2016, AJ, 152, 97
Wang, J. J., Ruffio, J.-B., De Rosa, R. J., et al. 2015, pyKLIP: PSF Subtraction for Exoplanets and Disks, ascl:1506.001
Wang, J. J., Vigan, A., Lacour, S., et al. 2021, AJ, 161, 148
Weigelt, G., Balega, Y., Preibisch, T., et al. 1999, A&A, 347, L15
Williams, J. P., & Cieza, L. A. 2011, ARA&A, 49, 67
Wu, Y.-L., Sheehan, P. D., Males, J. R., et al. 2017, ApJ, 836, 223
Yelda, S., Lu, J. R., Ghez, A. M., et al. 2010, ApJ, 725, 331
Zhou, Y., Bowler, B. P., Wagner, K. R., et al. 2021, AJ, 161, 244
Zurlo, A., Cugno, G., Montesinos, M., et al. 2020, A&A, 633, A119